Energy Materials and Devices

Review

# Review of all-inorganic perovskites and their tandem solar cells with crystalline silicon

Hongjun Wu, Zhaorui Sun, Haonan Li, Xiuhua Chen ✉, Wenhui Ma, Shaoyuan Li, Zhengjie Chen, and Fengshuo Xi

## Graphical Abstract

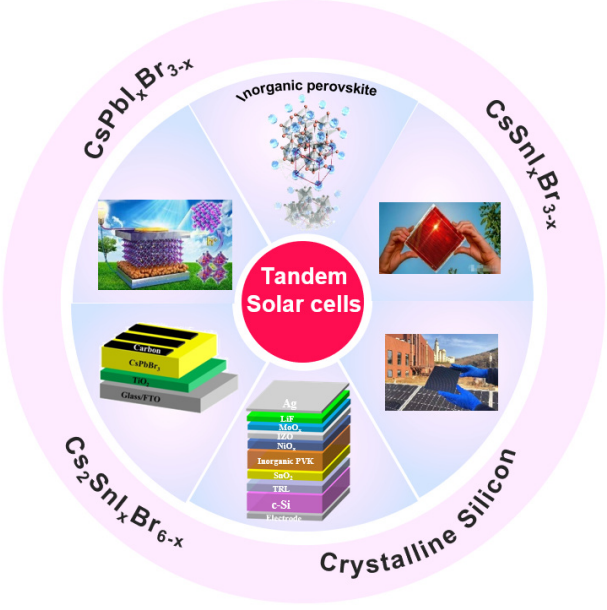


All-inorganic perovskite tandem solar cells can maintain the stability of material components within the device, preventing decomposition, and meeting the photovoltaic industry's design lifespan requirement of 25 years for large-scale commercial solar modules. This review is the first to address recent advancements in tandem solar cells that use all-inorganic perovskites and crystalline silicon.

✉Address correspondence to Xiuhua Chen, chenxh@ynu.edu.cn

**Received:** July 15, 2024
**Revised:** September 7, 2024
**Accepted:** September 19, 2024

Read Online

Submit Online

**Citation:** Wu H., Sun Z., Li H., et al. Review of all-inorganic perovskites and their tandem solar cells with crystalline silicon. *Energy Mater. Devices*, 2024, 2(3), 9370045. https://doi.org/10.26599/EMD.2024.9370045

Energy Materials and Devices

Open Access

Review

https://doi.org/10.26599/EMD.2024.9370045

# Review of all-inorganic perovskites and their tandem solar cells with crystalline silicon

Hongjun Wu[1,2], Zhaorui Sun[1], Haonan Li[1], Xiuhua Chen[1,2] ✉, Wenhui Ma[1], Shaoyuan Li[3], Zhengjie Chen[3], and Fengshuo Xi[3]

[1] *School of Materials and Energy, Yunnan University, Kunming 650500, China*
[2] *Institute of International Rivers and ECO-Security, Yunnan University, Kunming 650500, China*
[3] *School of Metallurgical and Energy Engineering, Kunming University of Science and Technology, Kunming 650500, China*

**Received:** July 15, 2024 / **Revised:** September 7, 2024 / **Accepted:** September 19, 2024

## ABSTRACT

In widely studied organic–inorganic hybrid perovskites, the organic component tends to volatilize and decompose under high temperatures, oxygen, and humidity, which adversely affects the performance and longevity of the associated solar cells. In contrast, all-inorganic perovskites demonstrate superior stability under these conditions and offer photoelectric properties comparable to those of their hybrid counterparts. The potential of tandem solar cells (TSCs) made from all-inorganic perovskites is especially promising. This review is the first to address recent advancements in TSCs that use all-inorganic perovskites and crystalline silicon (c-Si), both domestically and internationally. This work provides a systematic and thorough analysis of the current challenges faced by these systems and proposes rational solutions. Additionally, we elucidate the regulatory mechanisms of all-inorganic perovskites and their TSCs when combined with c-Si, summarizing the corresponding patterns. Finally, we outline future research directions for all-inorganic perovskites and their TSCs with c-Si. This work offers valuable insights and references for the continued advancement of perovskite-based TSCs.

## KEYWORDS

all-inorganic perovskites, single-junction solar cells, perovskite/crystalline silicon, tandem solar cells

## 1 Introduction

Recently, perovskite solar cells made from materials with tunable bandgaps and high defect tolerance have attracted considerable attention from researchers. Their advantages include superior light absorption coefficients, high carrier mobility, straightforward fabrication processes, and low cost, making them a popular research direction in the photovoltaic field. In 2009, Kojima et al.[1] pioneered the use of organic–inorganic hybrid perovskite materials in dye-sensitized solar cells, resulting in the first perovskite solar cell (PSC) with a photoelectric conversion efficiency (PCE) of 3.8%. In 2012, Kim et al.[2] used $CH_3NH_3PbI_3$ as the light absorption layer and 2,2′ ,7,7′ -tetrakis(*N*,*N*-di-*p*-methoxyphenylamine)-9,9′ -spirobifluorene (Spiro-OMeTAD) as the hole transport layer (HTL), achieving a solid-state PSC with an efficiency of 9.7%. Remarkably, this efficiency was maintained even after 500 h of storage without encapsulation. Over the past decade, the efficiency of single-junction PSC has surged from an initial 3.8% to 26.2%[3], with further improvements still possible.

Research has shown that the organic components in widely studied organic–inorganic hybrid PSC are highly susceptible to severe decomposition under high temperatures, oxygen, and humidity[4–7]. This decomposition compromises the perovskite photoactive layer, adversely affecting both the photoelectric properties and stability of the cells and ultimately damaging their integrity. For instance, the

✉ Address correspondence to Xiuhua Chen, chenxh@ynu.edu.cn

organic–inorganic hybrid perovskite material $MAPbI_3$ readily decomposes into $PbI_2$ and MAI, with MAI further breaking down into $CH_3NH_2$ and HI and potentially into $CH_3I$ and $NH_3$ at high temperatures[8]. In contrast, all-inorganic perovskite materials exhibit excellent thermal stability, maintaining their original components and crystal structure under similar environmental conditions[9]. Furthermore, solar cells made from all-inorganic perovskite materials have demonstrated excellent photoelectric properties comparable to those of hybrid PSC. This suggests that all-inorganic PSC are promising materials[10]. However, it is important to note that all solar cell materials are subject to a theoretical limit on their PCE, known as the Shockley–Queisser limit. For example, Richter et al.[11] calculated that the theoretical PCE limits for single-junction crystalline silicon (c-Si) solar cells and PSC are 29.4% and 33%, respectively. Currently, the PCE of commonly used single-junction solar cells is approaching its theoretical limit, leaving minimal room for further enhancement. However, tandem solar cells (TSCs), which use combinations of materials with different bandgaps, have the potential to exceed the theoretical PCE limits of single-junction cells. TSCs can achieve higher energy conversion efficiencies by effectively harnessing the photonic energy across multiple bands of the solar spectrum[12].

Given the importance and potential of integrating all-inorganic perovskites with c-Si to create TSCs, there remains a lack of comprehensive reviews on this topic both domestically and internationally. This review thoroughly examines and summarizes the current state of single-junction all-inorganic PSC and double-junction perovskite TSCs, focusing on key aspects such as component regulation, process optimization, and PCE enhancement, as well as the challenges faced. It also proposes practical solutions to these issues. Additionally, the review outlines future research directions for all-inorganic perovskites and their TSCs with c-Si, aiming to offer new research perspectives and valuable references for advancing next-generation all-inorganic perovskite TSCs.

## 2 Single-junction all-inorganic PSC

To date, most all-inorganic perovskite materials (with the general chemical formula $ABX_3$) typically use Cs as the A-site cation and Sn, Pb, or Ge as the B-site cations. The X-site anions are usually halogens such as I, Br, or their mixtures. This composition is primarily chosen to maintain a tolerance factor in the range of 0.8–1.1, which helps ensure the formation of a stable perovskite phase under conventional usage conditions[13,14]. The tolerance factor ($t$) can be used for assessing the stability of the perovskite crystal structure:

$$t = \frac{(r_A + r_X)}{\sqrt{2}(r_B + r_X)}$$

where $r_X$, $r_B$, and $r_A$ denote the ionic radii of the X, B, and A positions, respectively. Perovskite-type crystals are generally formed when $0.8 < t < 1.0$. If $t$ falls below 0.9, the perovskite crystal structure tends to distort, leading to instability. Inorganic perovskites often exhibit different crystal structure phases depending on environmental temperature, including cubic α-phase, tetragonal β-phase, orthorhombic γ-phase, and orthogonal δ-phase, with the δ-phase representing a non-perovskite structure. The following section will focus on the current research on $CsPbX_3$, $CsSnX_3$, and other series of single-junction all-inorganic PSC.

### 2.1 Single-junction lead-based all-inorganic PSC

Currently, the most common lead-based all-inorganic PSC include four main types: $CsPbI_3$, $CsPbI_2Br$, $CsPbIBr_2$, and $CsPbBr_3$ solar cells. The bandgap values for these perovskite materials are 1.73 eV, 1.92 eV, 2.05 eV, and 2.3 eV, respectively. A summary discussion of each of these solar cells is provided below.

#### 2.1.1 *$CsPbI_3$ solar cell*

The $CsPbI_3$ solar cell can achieve a high short-circuit current density ($J_{sc}$), but its commercialization has been limited by the poor stability of the untreated $CsPbI_3$ crystal structure. $CsPbI_3$ has three perovskite phases—α, β, and γ—collectively known as the black phase, which exhibit excellent optoelectronic properties. Conversely, the δ phase, also known as the yellow phase, does not have a perovskite structure and lacks optoelectronic properties. The α phase generally requires temperatures above 300 °C to remain stable. As the temperature decreases to approximately 281 °C, $CsPbI_3$ undergoes a phase transition from the black α-$CsPbI_3$ to the black β-$CsPbI_3$. Further cooling below 184 °C leads to the formation of the metastable black γ-$CsPbI_3$ phase. When exposed to humid conditions, γ-$CsPbI_3$ rapidly transforms into the nearly transparent, pale yellow δ-$CsPbI_3$, which lacks a perovskite structure. This δ phase has a bandgap of approximately 2.8 eV, considerably limiting its visible light absorption and rendering it unsuitable for photovoltaic applications. The temperature-induced phase transitions of $CsPbI_3$ are shown in Fig. 1[15].

The solar cell using $CsPbI_3$ as the light absorption layer initially achieved a PCE of only 0.09%[16]. In 2015, Eperon et al.[17] used HI to control the crystallization of $CsPbI_3$, resulting in smaller crystal sizes and a PCE of 2.9%. The addition of HI induces the formation of smaller crystal grains with increased

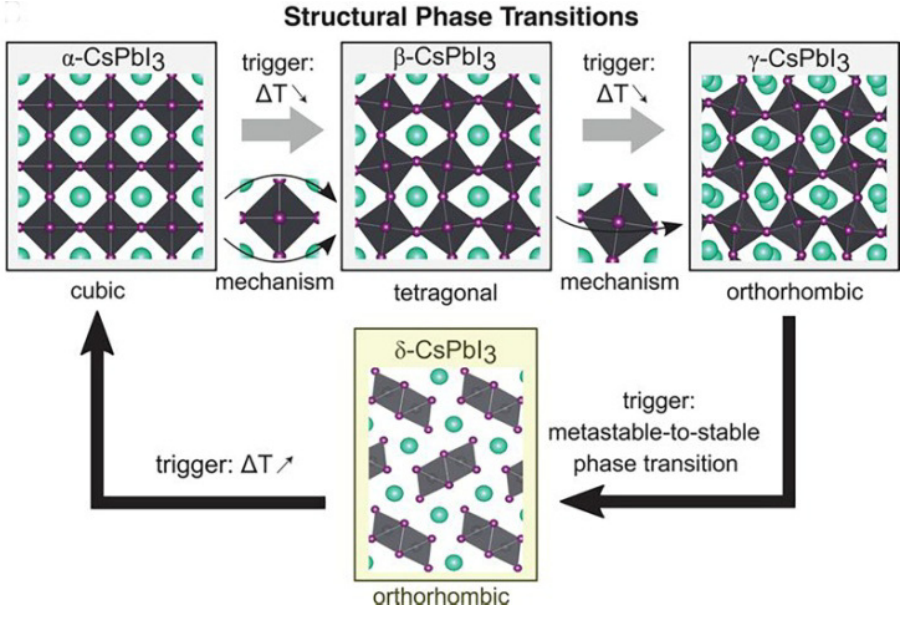


**Figure 1** Different crystal structure phases and their transformation process in $CsPbI_3$. Reproduced with permission from Ref. [15] ©2019, The American Association for the Advancement of Science.

lattice strain, enhancing the phase transformation stability of the perovskite at lower temperatures. Xiang et al.[18] replaced $PbI_2$ with $HPbI_3$ to create $CsPbI_3$ solar cells without an HTL. This adjustment reduced the bandgap of $CsPbI_3$ from 1.72 eV to 1.68 eV, resulting in a larger $J_{sc}$ and a PCE of 9.5%. The $CsPbI_3$ solar cell maintained good stability without substantial decomposition after being stored in dry air for 4 months. In 2016, Swarnkar et al.[19] demonstrated that nanocrystal surfaces can stabilize α-$CsPbI_3$ at ambient conditions, with the phase transformation temperature of $CsPbI_3$ quantum dots being considerably lower than that of bulk materials. This reduction is primarily attributed to quantum size and surface effects. Quantum dots, with their extremely small sizes (typically at the nanoscale), exhibit markedly different physical and chemical properties compared to bulk materials. Owing to their small size and high surface energy, $CsPbI_3$ quantum dots can have a less stable crystal structure, leading to phase transitions at lower temperatures. However, $CsPbI_3$ quantum dots can be stored at room temperature for several months without considerable degradation. Inorganic PSC made from $CsPbI_3$ quantum dots achieved a PCE above 10%. In 2022, Tan et al.[20] explored the thermal stability and performance of two-dimensional (2D) perovskites using three hydrophobic organic amine salts and examined their passivation effect on $CsPbI_3$. They discovered that phenyltrimethyl ammonium iodide (PTAI) and its corresponding 2D perovskite exhibited exceptional thermal stability. Further investigation revealed that the PTAI-based 2D perovskite primarily formed at grain boundaries, enhancing $CsPbI_3$ phase stability and effectively suppressing non-radiative recombination. As a result, they developed a $CsPbI_3$ solar cell with a record PCE exceeding 20% and high stability. To date, researchers have primarily used techniques such as ion doping, small molecule or polymer regulation of crystallite size, and surface passivation to stabilize the cubic phase during $CsPbI_3$ solar cell fabrication. Currently, the optimized $CsPbI_3$ PSC achieves a record PCE of 21.11%, retains 92.74% of its initial efficiency after 800 h of aging in an air atmosphere, and shows virtually no efficiency degradation after 350 h of maximum power point tracking[17–18,21–22].

### 2.1.2 *$CsPbBr_3$ solar cell*

The $CsPbI_3$ solar cell exhibits a high $J_{sc}$, but its performance is constrained by a low open-circuit voltage ($V_{oc}$) owing to the bandgap. Completely substituting $I^-$ with $Br^-$ results in the formation of a stable yellow orthorhombic γ-$CsPbBr_3$ perovskite with a bandgap of 2.3 eV at room temperature[23]. Kulbak et al.[24] fabricated a solar cell with the structure FTO/m-$TiO_2$/$CsPbBr_3$/HTL/Au using a two-step solution process. Using 4,4′-*N*,*N*′-dicarbazole-biphenyl (CBP), Spiro-OMeTAD, and poly[bis(4-phenyl)(2,4,6-trimethylphenyl)amine] (PTAA) as the HTL, they achieved PCEs of 4.72%, 4.98%, and 5.95%, respectively. Additionally, the thermal stability was considerably better than that of comparable $MAPbBr_3$ solar cells. However, the overall PCE of these $CsPbBr_3$ solar cells remained relatively low. This is primarily attributed to factors such as its bandgap, defect density, grain size, interface and internal charge recombination, and irreversible phase transitions. To enhance the performance of $CsPbBr_3$ solar cells, Tong et al.[25] developed a high-performance $CsPbBr_3$

solar cell by controlling the ratio of CsBr to $PbBr_2$ through gas phase growth, forming perovskite derivative phases ($CsPb_2Br_5$/$Cs_4PbBr_6$). This method not only ensures more uniform grain sizes in the perovskite films but also reduces the surface potential barriers between grains and grain boundaries. As a result, the PSC with an Ag electrode achieved a PCE of 10.91%. In 2020 and 2021, Zhou et al.[26,27] further explored strategies such as releasing interface strain and facilitating the coalescence of perovskite lattices to improve the performance of $CsPbBr_3$ solar cells. Initially, they introduced a $CsPbBr_3$-based PSC with a $WS_2$ interlayer (Figs. 2a and 2b). The grain size of the $CsPbBr_3$ film crystals was considerably enhanced after a simple spin coating of 2D tungsten disulfide ($WS_2$) layers (Figs. 2c and 2d). The "lubricating" effect of $WS_2$ nanosheets between the electron transport layer (ETL) and the perovskite, along with the formation of a $WS_2$/$CsPbBr_3$ van der Waals heterostructure, helped relieve interfacial strain and facilitated the condensation of the perovskite lattice. Consequently, the $V_{oc}$ and PCE of the $CsPbBr_3$ solar cell reached 1.70 V and 10.65%, respectively (Figs. 2e and 2f). Additionally, the device's stability was considerably enhanced. They then proposed a strategy to considerably reduce surface lattice tensile strain by incorporating an inorganic 2D Cl-terminated $Ti_3C_2$ ($Ti_3C_2Cl_x$) MXene into both the bulk and surface of the $CsPbBr_3$ film. The strong interactions between the Cl atoms in $Ti_3C_2Cl_x$ and the undercoordinated $Pb^{2+}$ in the $CsPbBr_3$ lattice compress and confine the expanded perovskite lattice in a "tape", where the Pb–Cl bonds act as a "glue" to stabilize the lattice structure. This approach led to an exceptionally high $V_{oc}$ of 1.702 V and a peak PCE of 11.08%. Furthermore, the device demonstrated remarkable stability, maintaining its performance without encapsulation for over 100 days in 80% relative humidity and for more than 30 days at 85 °C.

To enhance the photoelectric performance of $CsPbBr_3$ solar cells, Duan et al.[28] performed lattice doping of $CsPbBr_3$ with lanthanide ions ($Ln^{3+}$). Their study demonstrated that incorporating $Ln^{3+}$ into the perovskite lattice increased grain size and carrier lifetime, leading to a considerable increase in device performance. Notably, the $Sm^{3+}$-doped device achieved a $V_{oc}$ of 1.594 V, with its performance remaining stable even after 110 days of storage in an 80% humidity environment.

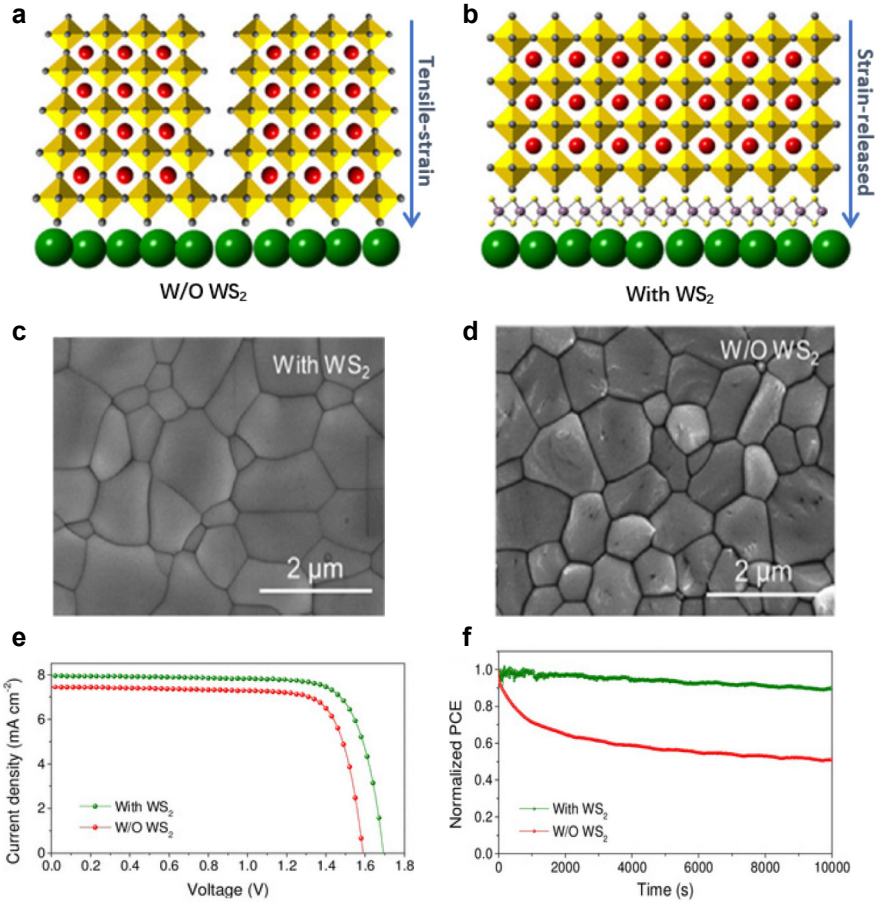


**Figure 2** Residual strain distribution in $CsPbBr_3$ grains without (a) and with (b) $WS_2$ modified layer. Top-view SEM images of $CsPbBr_3$ films with (c) and without (d) $WS_2$ nanosheet modification. *J-V* curve (e) and photostability (f) of the $CsPbBr_3$ solar cell with or without $WS_2$ interlayer under 1 standard sun illumination. Reproduced with permission from Ref. [26] ©2020, Wiley-VCH GmbH.

### 2.1.3 *$CsPbI_2Br$ solar cell*

Among common lead-based all-inorganic perovskites, $CsPbI_3$ possesses the most suitable bandgap, but its α-$CsPbI_3$ phase is highly unstable at room temperature. While $CsPbBr_3$ is more stable, it has a wider bandgap, which reduces $J_{sc}$ in solar cells made from it. To address this, partial $Br^-$ doping can substitute some of $I^-$ in $CsPbI_3$, adjusting the bandgap of the perovskite material and enhancing both its stability and photoelectric performance. Common $Br^-$-doped $CsPbI_3$ compounds include $CsPbI_2Br$ and $CsPbIBr_2$. $CsPbI_2Br$ solar cells, in particular, exhibit relatively high PCE and stability. $CsPbI_2Br$ can absorb photons with wavelengths shorter than 650 nm, resulting in a theoretical limiting $J_{sc}$ of approximately 17 mA/cm$^2$ for its corresponding solar cell. The tolerance factor of $CsPbI_2Br$ remains below 0.9 because only one $Br^-$ replaces $I^-$, making its crystal structure susceptible to phase transitions at room temperature. In recent years, researchers have investigated a range of promising and effective strategies to enhance the stability of $CsPbI_2Br$ solar cells.

First, Nam et al.[29] investigated how annealing temperature affects the chemical state and surface morphology of $CsPbI_2Br$ films during the crystallization process. They discovered that annealing temperature considerably influences the stability and PCE of the solar cell. The film exhibited optimal quality at an annealing temperature of 280 °C, showing a dense, pore-free surface (Fig. 3a).

Second, some researchers have investigated ion doping as a strategy to enhance the stability of $CsPbI_2Br$ solar cell. Fu et al.[30] doped the $F^-$ element into $CsPbI_2Br$ to form $CsPbBrI_{2-x}F_x$, which can alter the original perovskite crystal's tolerance factor and possibly form a bulk heterostructure, increasing its stability. The solar cell prepared with new perovskite retained approximately 70% of its initial PCE after being placed in air for 10 days. Bai et al.[31] added $MnCl_2$ to the precursor solution, with $Mn^{2+}$ entering the $CsPbI_2Br$ lattice gaps, inhibiting nucleation and slowing down crystallization rate, resulting in large-particle dense film while reducing surface defects. Moreover, due to the hydrophobic nature of $Cl^-$, it can effectively reduce the impact of moisture on perovskite film, and the solar cell still maintained 97% of its original PCE after being stored at 25 °C,

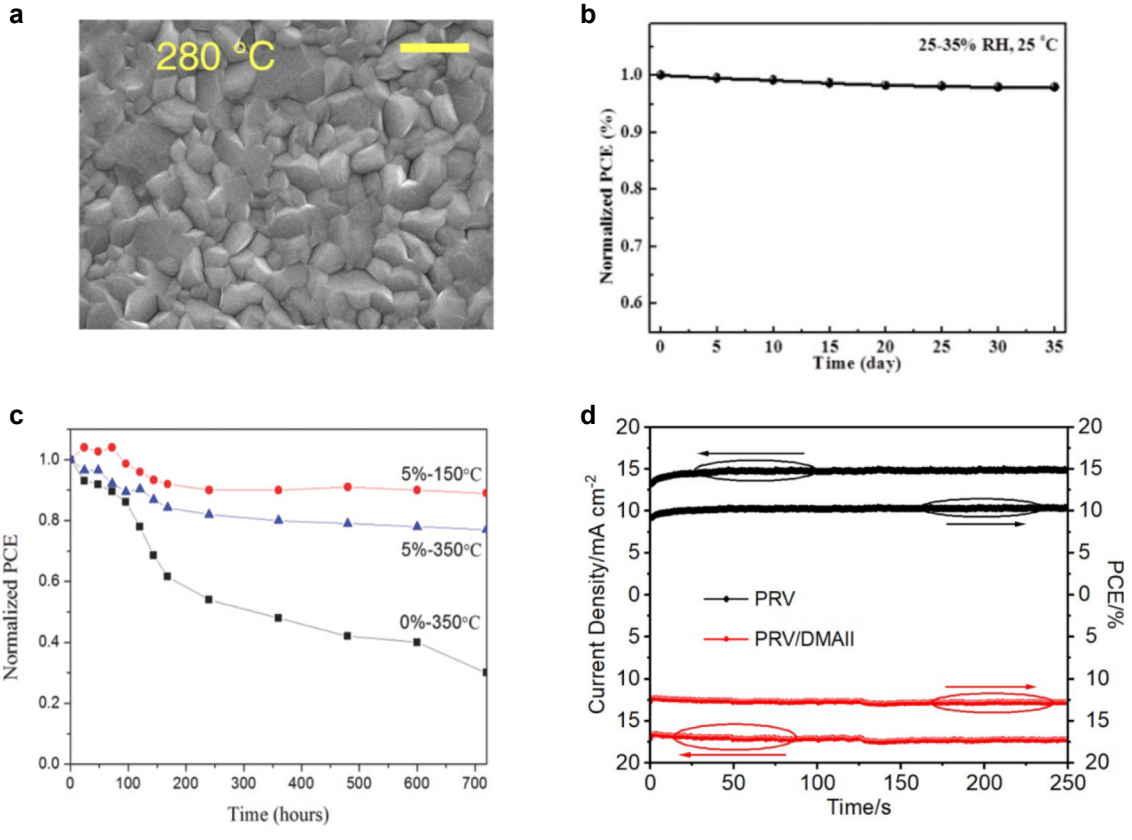


**Figure 3** (a) SEM image of $CsPbI_2Br$ film annealed at 280 °C. Reproduced with permission from Ref. [29] ©2017, American Chemical Society. (b)Long-term stability of best-performing solar cell without encapsulated storage. Reproduced with permission from Ref. [31] ©2018, American Chemical Society. (c) $CsPbI_2Br$ solar cell composition placement efficiency attenuation chart in air for 30 d. Reproduced with permission from Ref. [32] ©2018, WILEY-VCH Verlag GmbH & Co. KGaA, Weinheim. (d) PCE and steady-state output of photocurrent for $CsPbI_{3-x}Br_x$ PSC with (denoted as PRV/DMAII) and without (denoted as PRV) DMAII passivation. Reproduced with permission from Ref. [34] ©2022, American Chemical Society.

25% to 35% relative humidity for over 60 days (Fig. 3b). They further found that the perovskite material undergoes photoinduced phase separation, and with the increase of $Br^-$, the light stability decreases. Zeng et al.[32] added $CH_3COO^-$ to the precursor solution, where $CH_3COO^-$ controlled $CsPbI_2Br$ crystal growth, formed dense film by reducing grain size, and formed a PbO passivation film at the grain boundary surface after annealing. The prepared solar cell maintained 90% of its original PCE after being stored in air with 20% relative humidity for 30 days (Fig. 3c).

Furthermore, researchers have explored interface optimization techniques to enhance the stability of $CsPbI_2Br$ solar cells. Chen et al.[33] incorporated a 7.5 mg/mL solution of polyethylene oxide (PEO) into the $CsPbI_{3-x}Br_x$ film. The PEO acted as a passivator at the grain boundaries, and its high viscosity considerably improved the film-forming properties, reducing defects and enhancing surface uniformity. This approach considerably increased both the device's efficiency and stability. The unencapsulated devices achieved a maximum PCE of 10.95% and retained 98% of their initial PCE after 10 days of storage in a dark environment at 40% humidity and 25 °C. Zhao et al.[34] explored the use of 1,2-dimethyl-3-acetylimidazolium iodide (DMAII) applied via spin coating on the surface of $CsPbI_{3-x}Br_x$ perovskite films for fabricating PSC. They found that the DMAII layer provided dual benefits: surface passivation and phase stabilization. The DMAII passivation effectively reduced trap states in the $CsPbI_{3-x}Br_x$ perovskite film, improving hole extraction and minimizing charge recombination. The researchers evaluated the photocurrent and PCE of $CsPbI_{3-x}Br_x$ PSC before and after DMAII passivation under peak power conditions. After DMAII treatment, there was a considerable increase in the steady-state PCE, increasing from 10.40% to 12.88% (Fig. 3d), and the steady-state photocurrent increased from 15.245 to 17.500 mA/cm$^2$. Li et al.[35] discovered that applying a layer of poly(3-hexylthiophene-2,5-diyl) (P3HT) on $CsPbI_2Br$ effectively reduced surface defects, thereby decreasing the likelihood of photogenerated carrier recombination. They found that devices using both P3HT and Spiro-OMeTAD as organic hole transport layers exhibited similar PCEs, with the PCE remaining above 95% even after 1300 h in the environment. Additionally, they investigated the use of diphenylamine derivatives as a buffer layer to address the energy level mismatch between $CsPbI_2Br$ and P3HT. With the introduction of the buffer layer, the PCE of the undoped P3HT-based $CsPbI_2Br$ solar cell surpassed 15% owing to a reduction in $V_{oc}$ loss.

In summary, the photovoltaic performance of a $CsPbI_2Br$ solar cell is primarily determined by the quality of the thin film, its defect-free crystallinity, and its stability. Achieving a high-quality film requires accurate control over the growth process and subsequent annealing treatments. Interface engineering helps minimize surface defects and improve energy level alignment. Ion doping can enhance the layer's density and particle characteristics. Additionally, incorporating buffer and barrier layers can effectively mitigate moisture damage to the perovskite crystals, thereby improving both the stability and PCE of the solar cell.

#### 2.1.4 *$CsPbIBr_2$ solar cell*

The $J_{sc}$ limit for $CsPbIBr_2$ solar cells is approximately 13.5 mA/cm$^2$. These cells exhibit good stability owing to the 2:1 ratio of $Br^-$ to $I^-$. However, as reported in a previous study[34], photoinduced phase separation occurs in $CsPb(Br_xI_{1-x})_3$ when $x > 0.4$, leading to slow progress in improving solar cell PCE. Consequently, there is relatively limited research on $CsPbIBr_2$ solar cells. Ma et al.[36] fabricated a device with the structure/FTO/c-$TiO_2$/$CsPbIBr_2$/Au, achieving a PCE close to 5%. The primary limitation in the PCE of $CsPbIBr_2$ solar cells is phase separation caused by the high $I^-$ concentration. To address this issue, Zhu et al.[37] spin-coated CsI onto the surface of the $CsPbIBr_2$ precursor film, achieving a PCE of 9.16% for carbon-based $CsPbIBr_2$ solar cells without an HTL. This improvement is attributed to enhanced crystallinity and reduced crystal defects. Doping and interface modification are effective techniques for modifying crystalline properties and minimizing defects. Jiang et al.[38] added CsAc and $HPbX_3$ to the precursor solution to address the low solubility of CsBr, resulting in a $CsPbIBr_2$ film with a thickness of 500 nm. They also used phenylethylammonium iodide (PEAI) for surface passivation, which considerably decreased the defect state density of the quasi-2D perovskite formed. This led to a solar cell with a PCE of 12.4%. Currently, relatively efficient $CsPbIBr_2$ solar cells are achieved through Sn doping, which modifies the bandgap of the material owing to the presence of $Sn^{2+}$, resulting in an increased $J_{sc}$ of 14.3 mA/cm$^2$ and a final PCE exceeding 11%[39]. Although $CsPbIBr_2$ solar cells exhibit good stability, improving their PCE remains challenging. Despite adjustments in crystallization kinetics through methods such as doping, the solar cells still experience considerable hysteresis effects. To further enhance the PCE of $CsPbIBr_2$ solar cells, it is crucial to improve carrier extraction and transport by reducing grain boundaries and increasing grain size, which helps to minimize energy losses.

Table 1 summarizes and organizes the results of lead-based inorganic PSC using various experimental optimization methods, along with their respective conversion efficiencies.

### 2.2 Single-junction tin-based all-inorganic PSC

The development of tin-based PSC began somewhat

**Table 1** Various structures of lead-based inorganic perovskite solar cells and their conversion efficiencies

| Methods | Device structure | $\eta$/% | Remarks | Ref. |
|---|---|---|---|---|
| Preparation technology | ITO/$PbCl_2$-ZnO/$CsPbI_2Br$/PM6/$MoO_3$/Ag | 17.46 | Reduce defect | [43] |
| | FTO/c-$TiO_2$/m-$TiO_2$/$CsPb_{0.9}Sn_{0.1}IBr_2$/Carbon | 11.33 | Two-step spin coating | [39] |
| | FTO/bl-$TiO_2$/mp-$TiO_2$/$CsPb(I_xBr_{1-x})_3$/Spiro-OMeTAD/Au | 12.50 | Two-step spin coating | [46] |
| | FTO/$TiO_2$/$CsPbI_3$/Spiro-OMeTAD/Ag | 18.94 | Two-step spin coating | [53] |
| | FTO/$SnO_2$-$TiO_xCl_{4-2x}$/$CsPbBr_3$:$Ti_3C_2Cl_x$/Carbon | 11.08 | Multistep spin coating | [27] |
| | FTO/c-$TiO_2$/m-$TiO_2$/$CsPbBr_3$/Carbon | 9.59 | Organic solvent addition | [49] |
| | FTO/$SnO_2$/$CsPbI_2Br$/Spiro-OMeTAD/$MoO_3$/Ag | 17.10 | Organic solvent addition | [40] |
| | ITO/c-$TiO_2$/$CsPbIBr_2$/Spiro-OMeTAD/Ag | 11.49 | Organic solvent addition | [55] |
| | ITO/$SnO_2$/$CsPbI_2Br$/Spiro-OMeTAD/Au | 10.40 | Organic solvent addition | [45] |
| | FTO/$TiO_2$/$CsPbI_2Br$/Spiro-OMeTAD/Au | 14.78 | Organic solvent addition | [54] |
| | FTO/$TiO_2$/γ-$CsPbI_3$/Spiro-OMeTAD/Au | 18.56 | Reduce defect | [56] |
| | FTO/$TiO_2$/$CsPbI_2Br$/Spiro-OMeTAD/Au | 13.54 | Low-temperature deposition | [41] |
| | FTO/c-$TiO_2$/PTI-$CsPbBr_3$/Spiro-OMeTAD/Au | 10.91 | Gas phase growth method | [25] |
| Interface modification | FTO/$SnO_2$-$TiO_xCl_{4-2x}$/$WS_2$/$CsPbBr_3$/Carbon | 10.65 | Modified lattice | [26] |
| | FTO/c-$TiO_2$/$CsPbI_3$/OAI/Spiro-OMeTAD/Au | 19.80 | Reduce defect | [42] |
| | ITO/$SnO_2$/ZnO/$CsPbI_2Br$/Spiro-OMeTAD/$MoO_3$/Ag | 14.05 | Energy level match | [51] |
| | FTO/HTLs/$CsPbI_3$/PCBM/BCP/Ag | 18.89 | Energy level match | [60] |
| | FTO/c-$TiO_2$/$CsPb_{0.97}Tb_{0.03}Br_3$/SnS:ZnS/$NiO_x$/Carbon | 10.26 | Widening absorption | [52] |
| Element doping | FTO/$TiO_2$/$CsPbI_2Br$/Carbon | 15.12 | Increase stability | [44] |
| | FTO/$TiO_2$/$CsPbBrI_2$/$CsPbI_2Br$ QDs/PTAA/Au | 13.47 | Reduce defect | [31] |
| | ITO/$SnO_2$/$CsPbIBr_2$/Spiro-OMeTAD/Au | 15.54 | Dual-source thermal evaporation | [48] |
| | FTO/c-$TiO_2$/$CsPbI_2Br$/Carbon | 10.00 | Organic solvent addition | [57] |
| | FTO/c-$TiO_2$/α-$CsPb_{1-x}Bi_xI_3$/CuI/Au | 13.21 | Reduce defect | [61] |
| | FTO/c-$TiO_2$/m-$TiO_2$/$CsPbBr_3$/Spiro-OMeTAD/Ag | 6.30 | Reduce defect | [58] |
| | FTO/$TiO_2$/$CsPbIBr_2$/Spiro-OMeTAD/Au | 9.89 | Modified lattice | [47] |
| | FTO/$SnO_2$/$CsPbBr_3$/Carbon | 9.54 | Modified lattice | [50] |
| | FTO/c-$SnO_2$/$CsPb(I_{0.75}Br_{0.25})_3$-0.5FAOAc/Spiro-OMeTAD/Au | 17.00 | Modified lattice | [59] |

later than that of lead-based PSC. Replacing Pb in lead-based all-inorganic perovskites with Sn results in tin-based all-inorganic perovskites, which offer suitable bandgaps, extended spectral absorption ranges, and advantages such as low toxicity and minimal environmental impact. These attributes present a promising pathway for creating environmentally friendly and efficient PSC. Over a short period, tin-based all-inorganic perovskites have evolved from initial single structures to various high-performance variants. In addition to allowing accurate control over their internal electronic structures, these materials can be further optimized through the use of different additives and external fabrication conditions, leading to continuous improvements in material quality and solar cell performance.

Currently, the most common lead-based all-inorganic PSC are $CsSnI_3$, $CsSnI_2Br$, $CsSnIBr_2$, and $CsSnBr_3$ solar cells. The bandgap values for these four perovskite materials range from approximately 1.30 eV to 1.75 eV, which are lower than those of their corresponding lead-based all-inorganic perovskites. This makes them theoretically more suitable for PSC. However, in these tin-based all-inorganic perovskites, tin ions are predominantly in the $Sn^{2+}$ state. Because $Sn^{2+}$ is prone to oxidation to $Sn^{4+}$, this leads to the formation of Sn vacancies and subsequent p-type doping. The higher the concentration of Sn vacancies ($V_{Sn}$), the more pronounced the resulting p-type doping effect, which leads to an increased dark carrier density. Consequently, it is recommended to use alternative tin-based all-inorganic perovskites formed with $Sn^{4+}$, such as $Cs_2SnX_6$, for solar cell fabrication[62]. The following sections will review various types of single-junction tin-based all-inorganic PSC, including $CsSnI_3$, $CsSnBr_3$, $CsSnI_{3-x}Br_x$, and $Cs_2SnX_6$.

### 2.2.1 *$CsSnI_3$ solar cell*

$CsSnI_3$, a perovskite crystal material with a high light absorption coefficient (approximately $10^4$ $cm^{-1}$ in the visible range) and a low exciton binding energy (approximately 18 meV) exhibits four distinct phases at different temperatures, as illustrated in Fig. 4a[63]. The reaction between CsI and $SnI_2$ melts produces a high-temperature black cubic phase ($Pm\bar{3}m$, B-α) at temperatures between 227 °C and 435 °C. As the temperature decreases, this cubic phase transforms sequentially into a tetragonal phase (P4/mbm, B-β) at 107 °C and then into an orthorhombic phase (Pnma,

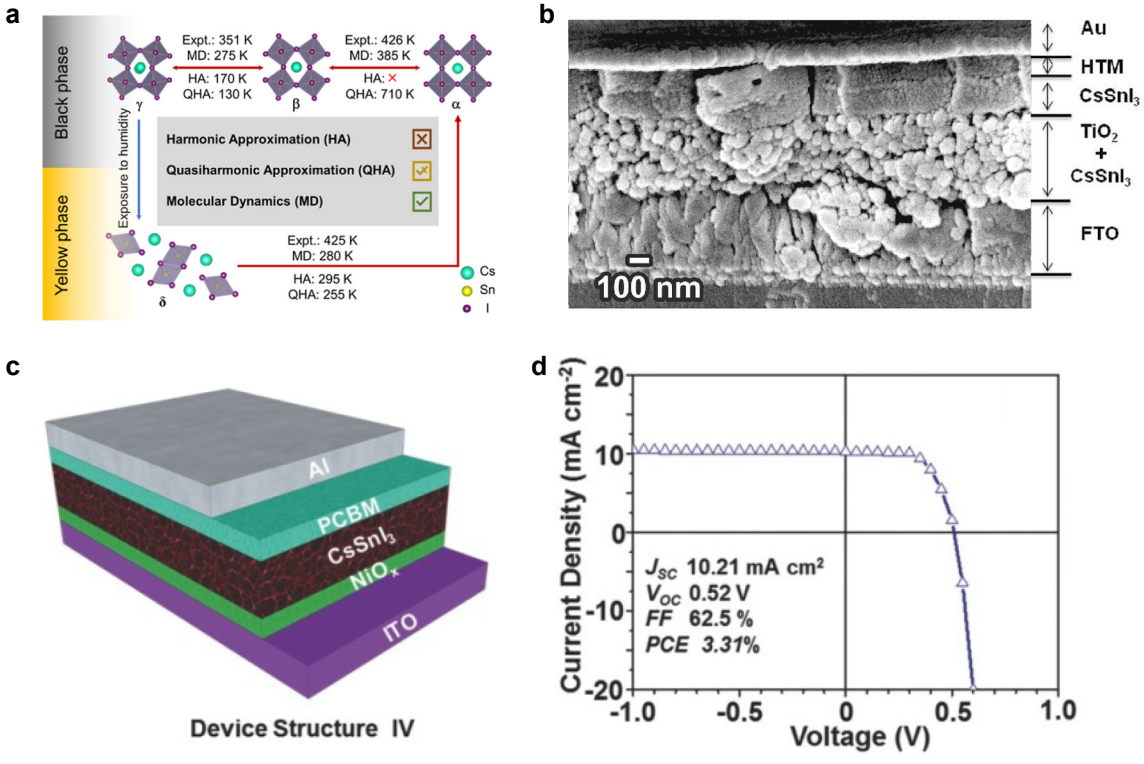


**Figure 4** (a) A phase transition diagram for $CsSnI_3$. Reproduced with permission from Ref. [63] ©2022, American Chemical Society. (b) SEM of $CsSnI_3$ solar cell. Reproduced with permission from Ref. [65] ©2014, WILEY-VCH Verlag GmbH & Co. KGaA, Weinheim. (c) Scheme of the $CsSnI_3$ solar cell. (d) *J*–*V* curve of $CsSnI_3$ solar cell. Reproduced with permission from Ref. [69] ©2016, WILEY-VCH Verlag GmbH & Co. KGaA, Weinheim.

B-γ) at 27 °C. At room temperature, the B-γ phase can readily transition to a yellow orthorhombic phase (Pnma, Y) in air, but it can revert to the B-α phase when reheated to above 152 °C in an inert gas. At room temperature, the Y phase, characterized by a tin iodide octahedral pseudo-one-dimensional double-chain structure, is the most stable. In contrast, the octahedral 3D connected B-γ phase is metastable. Exposure to oxygen or water vapor in the ambient air can induce the transformation of the B-γ phase to the Y phase, which negatively affects light absorption. Additionally, the Y-$CsSnI_3$ phase can further decompose into zero-dimensional $Cs_2SnI_6$ owing to the oxidation of $Sn^{2+}$ to $Sn^{4+}$.

Early on, Jokar et al.[64] demonstrated a Schottky solar cell using $CsSnI_3$ as the light absorption layer (ITO/$CsSnI_3$/Au/Ti). The $CsSnI_3$ layer was deposited via a vacuum evaporation method, with CsI and $SnCl_2$ alternately deposited and annealed at 175 °C. However, the solar cell's PCE was relatively low, at 0.88%. Kumar et al.[65] developed a solar cell structure with a $CsSnI_3$ film as the light absorption layer, as illustrated in Fig. 4b. They used a one step solution method to deposit the $CsSnI_3$ layer at 70 °C and found that the solvent considerably influenced the morphology of the $CsSnI_3$ layer. Compared to dimethylformamide (DMF) and 2-methoxyethanol, dimethyl sulfoxide (DMSO) enhanced the formation of an amorphous $TiO_2$ scaffold with better pore filling. High $V_{Sn}$ was identified as a major factor contributing to high background carrier concentration and charge recombination. The use of $SnF_2$ as an additive effectively reduced the $V_{Sn}$ concentration without incorporating it into the $CsSnI_3$ lattice. Adding 20% $SnF_2$ improved the photoelectric properties, resulting in a final solar cell with a $J_{sc}$ of 22.70 mA/cm$^2$, a $V_{oc}$ of 0.24 V, and a fill factor (FF) of 0.37. Mechanistic studies indicate that while there are no considerable energy barriers in the $CsSnI_3$ solar cell, recombination mechanisms still exist, which contribute to its relatively low PCE. On the one hand, PSC based on $CsSnI_3$ are prone to conventional intramolecular and interfacial defects, which lead to the recombination of photogenerated electrons and holes. On the other hand, as previously discussed, all Sn ions in $CsSnI_3$ are in the +2 oxidation state, making them vulnerable to oxidation to the +4 state. This oxidation generates Sn vacancies, introducing additional recombination pathways and centers. Consequently, the increased recombination rate results in more photogenerated carriers being lost before reaching the electrodes, reducing both the $V_{oc}$ and $J_{sc}$ and ultimately decreasing the device's PCE.

Marshell et al.[66] studied the preparation of $CsSnI_3$ perovskite films at room temperature and evaluated different tin halide reducers for use in solar cells.

Their findings indicated that $CsSnI_3$ films prepared at room temperature exhibited lower defect density and maintained some photoelectric performance even without additional Sn in the precursor solution. Adding $SnI_2$ to the precursor solution further enhanced the PCE of the $CsSnI_3$ solar cell. When a perovskite film with excess $SnI_2$ was paired with a $C_{60}$ layer, the hole mobility at the $CsSnI_3/C_{60}$ interface improved, resulting in a higher $V_{oc}$ for the device. The device with 10% excess $SnI_2$ achieved the highest PCE of nearly 3% when combined with 3 mg/mL indene–$C_{60}$ bisadduct (ICBA) and CuI and the highest $V_{oc}$ value of 0.55 V at a concentration of 5 mg/mL ICBA. The performance of the PSC is influenced by both the quality of the perovskite film and the device structure, with film quality being dependent on the preparation of the perovskite precursor solution[67]. Shao et al.[68] synthesized $CsSnI_3$ perovskite powders using the melt-cooling method and prepared the perovskite precursor via direct dissolution. They reported that increasing the annealing temperature of the $CsSnI_3$ film improved grain growth and crystallinity. However, this approach also increased the number of grain boundary trenches, produced more holes, and led to higher film roughness and $V_{Sn}$. The study ultimately determined that 150 °C was the optimal temperature for enhancing the performance of $CsSnI_3$ solar cells. Wang et al.[69] investigated the preparation of lead-free PSC heterostructures using coarse-grained B-γ-$CsSnI_3$ film. They found that the mesoporous $TiO_2$ and $Al_2O_3$ substrates negatively affected the photoelectric performance. For example, the insufficient coverage of the thinner $CsSnI_3$ layer (120 nm) on the mesoporous layer resulted in direct contact between the ETL and HTL. Additionally, the constraints imposed by the crystallized substrates, suboptimal solid–solid interfaces, and the presence of low-crystallinity impurities such as Y-$CsSnI_3$ and $Cs_2SnI_6$ on the substrates accelerated charge recombination, which was attributed to the low crystallinity of the B-γ phase $CsSnI_3$. Therefore, without adding any tin halides, the inverted structure PSC prepared using $NiO_x$ HTL and PCBM ETL exhibited $V_{oc}$, $J_{sc}$, and FF of 0.52 V, 10.21 mA/cm², and 0.625, respectively, as shown in Figs. 4c and 4d.

### 2.2.2 *$CsSnBr_3$ solar cell*

Incorporating $Br^-$ into $CsSnI_3$ instead of $I^-$ can enhance the $V_{oc}$ of the resulting solar cell. When $I^-$ is fully replaced by $Br^-$, the material's bandgap increases by 38.5%, and the absorption spectrum blueshifts. This substitution causes a structural transition from the orthorhombic phase of $CsSnI_3$ to the cubic phase of $CsSnBr_3$. Additionally, the presence of $Br^-$ reduces the number of Sn cation vacancies in the material. Compared to $I^-$, $Br^-$ integration results in a negligible perovskite layer on the mesoporous $TiO_2$ film. Experimental results indicate that a thinner layer consisting only of HTL improves the device's FF more effectively than a thicker layer containing both HTL and perovskite. Consequently, devices rich in $Br^-$ exhibit a higher FF than those rich in $I^-$[70,71]. Kumar et al.[72] incorporated graphene oxide into the preparation of $CsSnBr_3$ solar cells. They discovered that the addition of graphene oxide to the perovskite layer improved photon absorption, increased surface roughness, and enhanced the crystal quality of the nanocomposite material. This approach led to a solar cell with a PCE of 5.27%, a $V_{oc}$ of 0.714 V, a $J_{sc}$ of 12.04 mA/cm², and an FF of 0.61. Meanwhile, Kholil et al.[73] examined the structural, elastic, electronic, and optical properties of metal-doped $CsSnBr_3$ (with Mo/Tc). They found that metal doping resulted in a narrow-bandgap of 0.806 eV, which enhanced absorption and conductivity across 44% of the visible solar spectrum, thereby improving optical performance. Additionally, the metal-doped $CsSnBr_3$ showed high dielectric constants and low charge carrier recombination rates. Comparing the key properties of pure $CsSnBr_3$ with Mo-doped and Tc-doped versions indicates that $CsSn_{1-x}Tc_xBr_3$ (where $x = 0.125$) is the most promising environmentally friendly metal halide perovskite for use in solar cells and other optoelectronic applications.

### 2.2.3 *$CsSnI_{3-x}Br_x$ solar cell*

To address the issue of low output voltage in $CsSnX_3$ series solar cells, researchers have investigated halogen doping or substitution methods to enhance the device's output voltage by modifying the material's energy band structure. Sabba et al.[70] improved the $V_{oc}$ of their solar cells and achieved higher $J_{sc}$ by adjusting the ratio of $Br^-$ to $I^-$ in $CsSnI_{3-x}Br_x$ ($0 \le x \le 3$). They found that $Br^-$ doping reduced Sn vacancies in $CsSnI_{3-x}Br_x$ and caused a structural transition from orthorhombic $CsSnI_3$ to cubic $CsSnBr_3$, which led to increased output voltage with higher $x$ values. Raoui et al.[74] used SCAPS simulation software to examine how varying $Br^-$ contents in $CsSnI_{3-x}Br_x$ ($0 < x < 3$) affected the bandgap and the concentration of defects at the absorption layer interface. They also evaluated the PCE of PSC using different HTL materials, including CuSCN, PTAA, and Spiro-OMeTAD. It is worth noting that an HTL is not always necessary for tin-based PSC. Previous research has indicated that PSC using carbon as an electrode can exhibit good air stability without an HTL owing to the hydrophobic properties of the carbon electrode[75]. In a similar approach, Li et al.[76] used carbon as the electrode and omitted the HTL. They stabilized $Sn^{2+}$ in the tin-based perovskite using a novel additive, *trans*-DACH, which mitigated the self-doping effect of $Sn^{2+}$. This approach enabled the production of consistent perovskite precursor solutions and

uniform, compact perovskite films even in high humidity conditions. Consequently, the solar cell demonstrated enhanced light absorption, reduced defects, and improved carrier transport capabilities. Additionally, after being stored in ambient air for over 160 h, the device retained 73.7% of its initial PCE.

### 2.2.4 $Cs_2SnX_6$ solar cell

Currently, research and application of double perovskite materials, such as $A_2B_2X_6$ and $A_2BX_6$, in solar cells are still in the early stages. There is limited information available on the types, properties, internal mechanisms, and preparation processes of these materials. This section will specifically discuss $Cs_2SnI_6$ (Fig. 5)[77], which features a straightforward ionic structure.

Compared to conventional tin-based perovskites such as $CsSnX_3$, the Sn ions in $Cs_2SnI_6$ are in a more stable +4 oxidation state, which enhances the stability of $Cs_2SnI_6$ in air and humid environments. The $Cs_2SnI_6$ layer effectively protects the underlying $CsSnI_3$ film from decomposition. As a result, the corresponding solar cell retains 90% of its initial PCE after 20 h of storage under natural environmental conditions, considerably improving the stability of $CsSnI_3$ PSC. Additionally, unlike other tin-based perovskites, the strong covalent Sn–I bonds in $Cs_2SnI_6$ contribute to a high enthalpy change ($\Delta H$ > 3.6 eV), making the formation of Sn vacancies in $Cs_2SnI_6$ less likely[78,79]. As discussed, Sn in $Cs_2SnI_6$ is in a +4 valence state, which not only provides high stability against water and oxidation but also acts as a p-type dopant in the material. This dual role enhances the stability of solar cells and helps reduce device fabrication costs[80,81]. Literature reports indicate that $Cs_2SnI_6$ powder, with a bandgap of 1.48 eV and a high light absorption coefficient, maintains its morphology and structure for over a week to a month in high humidity conditions and remains stable up to 270 °C[82,83]. Additionally, field-effect transistors based on $Cs_2SnI_6$ nanocrystals exhibit infrared photoluminescence and p-type conduction behavior in ambient air, with hole mobility exceeding 20 $cm^2/(V{\cdot}s)$. This series of properties indicates that $Cs_2SnI_6$ is suitable for the preparation of solar cells.

Similar to other conventional tin-based perovskites, the performance of $Cs_2SnI_6$ and its solar cells can be optimized through component engineering and refinement of preparation techniques. Component engineering primarily involves adjusting halogen composition and content. For example, Lee et al.[80] developed a series of $Cs_2SnI_{6-x}Br_x$ perovskite materials with bandgap values ranging from 1.3 eV to 2.9 eV using a two-step solution synthesis method. When $x$ = 2, the device's PCE exceeded 2%. Additionally, the optimization of solar cell structure and preparation processes is crucial. Murshed et al.[84] reported preparing $Cs_2SnI_6$ film using a 0.4 mol solution of $SnI_2$ and CsI (with 20% $SnF_2$) in γ-butyrolactone (GBL) solvent, with chlorobenzene added as an antisolvent. The film was tested with solvents such as DMSO and DMF to examine the phase formation and morphology control of the perovskite. The final lead-free planar PSC demonstrated a $J_{sc}$ of 9.28 $mA/cm^2$, $V_{oc}$ of 0.81 V, and FF of 0.68, indicating excellent performance. Additionally, $Cs_2SnI_6$ film prepared via aerosol-assisted chemical vapor deposition (AACVD) exhibited purer crystal phases (fewer CsI impurities) and superior air stability compared to those produced by spin coating. The AACVD-grown $Cs_2SnI_6$ film had a 1.3 eV bandgap and a uniform surface morphology. After being stored in the air for 100 days, the film retained high phase purity. This stability is attributed to the passivation effect of $SnI_4$ in the precursor vapor, which prevented decomposition and thereby enhanced the stability of both the $Cs_2SnI_6$ film and its solar cell[85–87].

Table 2 summarizes and organizes the results of tin-based inorganic PSC using various experimental optimization methods, along with their respective conversion efficiencies.

## 3 Perovskite TSCs

One of the key features of perovskites is their tunable bandgap. Through composition control, both hybrid and inorganic perovskites can achieve bandgaps ranging from 1.3 eV to 2.3 eV or even wider[96].

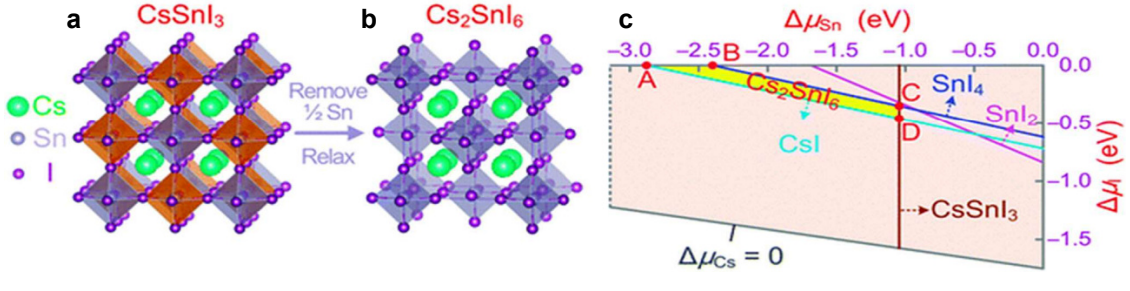


**Figure 5** Crystal structure and chemical potential-phase map of $CsSnI_3$ and $Cs_2SnI_6$. Reproduced with permission from Ref. [77] ©2015, Royal Society of Chemistry.

**Table 2** Various structures of tin-based inorganic perovskite solar cells and their corresponding conversion efficiencies

| Methods | Device structure | $\eta$/% | Remarks | Ref. |
|---|---|---|---|---|
| Element doping | FTO/$TiO_2$/$CsSnI_3$/P3HT/Ag | 6.11 | Reduce defect | [88] |
| | c-$TiO_2$/m-$TiO_2$/$Al_2O_3$/$CsSnI_3$/NiO/Carbon | 8.03 | Reduce defect | [91] |
| | ITO/$SnO_2$/$CsSnI_{2.6}Br_{0.4}$/PCBM/Ag | 11.20 | Reduce defect | [95] |
| | FTO/$TiO_2$/$Al_2O_3$/$CsSnIBr_2$/Spiro-OMeTAD/Au | 3.20 | Adding organic solvent | [89] |
| Preparation technology | ITO/Zn(O,S)/$Cs_2SnI_6$/Carbon/Au | 5.18 | One step scraper method | [84] |
| | ITO/$TiO_2$/$Al_2O_3$/$CsSnI_3$/NiO/Carbon/Ag | 8.27 | Adding inorganic solvent | [94] |
| | FTO/N719 dyed $TiO_2$/$Cs_2SnI_6$/Pt/FTO | 6.32 | Adding organic solvent | [78] |
| | FTO/c-$TiO_2$/N719 adsorbed m-$TiO_2$/ KI-3D/ $Cs_2SnI_6$/Pt/FTO | 5.89 | Adding organic solvent | [90] |
| | FTO/ZnO/rGO-$CsSnBr_3$/$Cu_2O$/Ag | 5.27 | Adding graphene oxide | [72] |
| | FTO/$TiO_2$/$Cs_2SnI_{6-x}Br_x$/HTL/Ag | 3.20 | One step solution | [93] |
| | Ag/PCBM/$CsSnI_3$/PCBM/Ag | 11.70 | Reduce defect | [92] |
| | ITO/PEDOT: PSS/$CsSnI_3$/$PC_{61}BM$/BCP/Ag | 6.53 | Single crystal precursor | [67] |
| | FTO/m-$TiO_2$/$Cs_2SnI_6$/N719-dye/Pt | 6.75 | Spin coating | [81] |
| | ITO/PEDOT:PSS/$EA_{0.08}$2D/3D $CsSnI_3$/$C_{60}$/BCP/Al | 7.70 | Ethylamine hydroiodide | [68] |

Generally, all-inorganic perovskites, whether lead-based or tin-based, have relatively wide bandgaps, resulting in a narrower spectral response range. This narrower range leads to a lower photocurrent density in single-junction solar cells, thereby impacting the overall PCE. In contrast, c-Si solar cells, which dominate over 90% of the photovoltaic market, have a narrower silicon bandgap of 1.12 eV, allowing them to absorb sunlight across a broad spectrum from 300 to 1200 nm. Currently, the highest commercial PCE for highly efficient n-type single-crystal silicon solar cells with a single-junction has reached 26.89%[97]. In 2024, *LONGi*, a leading solar company, reported a new laboratory record PCE of 27.3% for silicon heterojunction back-contact cells[98]. This achievement is nearing the theoretical limit of 29.4% for c-Si solar cells[11]. This demonstrates that there is a maximum potential for PCE improvement in single-junction solar cells, regardless of the material used. TSC technology offers a promising approach to surpassing this theoretical PCE limit of single-junction solar cells. Figures 6a and 6b show the photon absorption and loss mechanisms in the solar spectrum for both single-junction solar cells and TSCs[99].

The principle behind enhancing PCE using TSC technology involves splitting the solar spectrum and stacking materials that absorb different light wavelengths. In this approach, materials with varying bandgaps are stacked from top to bottom. The top cell, made from a wide-bandgap material, captures short-wavelength, high-energy photons, while the bottom cell, composed of a narrow-bandgap material, absorbs long-wavelength, low-energy photons. This arrangement leverages the complementary advantages of each material, allowing for more efficient utilization of the entire spectrum of photonic energy. Stacking types in TSCs can generally be categorized into double- and multi-junctions. Theoretically, multi-junction TSCs offer a higher potential PCE compared to double-junction TSCs. However, their preparation is more complex and costly, which hinders large-scale commercial applications. Consequently, researchers are focused on optimizing double-junction TSCs to balance cost and PCE advantages. The following sections will primarily discuss double-junction TSCs.

## 3.1 Double-junction TSCs

### *3.1.1 Classification by material types*

Double-junction perovskite TSCs can be categorized into three types based on the materials used for the upper and lower sub-cells: (1) combinations of perovskite with rare metals such as germanium and gallium; (2) combinations of perovskite with other perovskites; and (3) combinations of perovskite with c-Si. Type 1 TSCs are typically reserved for specialized applications, such as defense and aerospace, owing to the high cost and rarity of the materials. Type 2 TSCs, which use perovskite materials in both sub-cells, have a theoretical maximum PCE exceeding 42%[100]. The materials for these cells are usually thin-film crystals, often grown on substrates such as glass. Owing to the very thin film thickness, perovskite/perovskite TSCs tend to have more defects and experience greater attenuation compared to perovskite/c-Si TSCs. This presents additional challenges that need to be addressed in future studies. Overall, the path to optimizing perovskite/perovskite stacking is longer and more complex. In contrast, for double-junction TSCs using the perovskite/c-Si combination, the bandgap of c-Si is 1.12 eV. Theoretical calculations suggest that when paired with an optimal bandgap perovskite material at 1.73 eV, the theoretical maximum PCE for such double-junction TSCs could reach up to 43%[101]. This makes the perovskite/c-Si route a promising avenue for large-scale commercial applications.

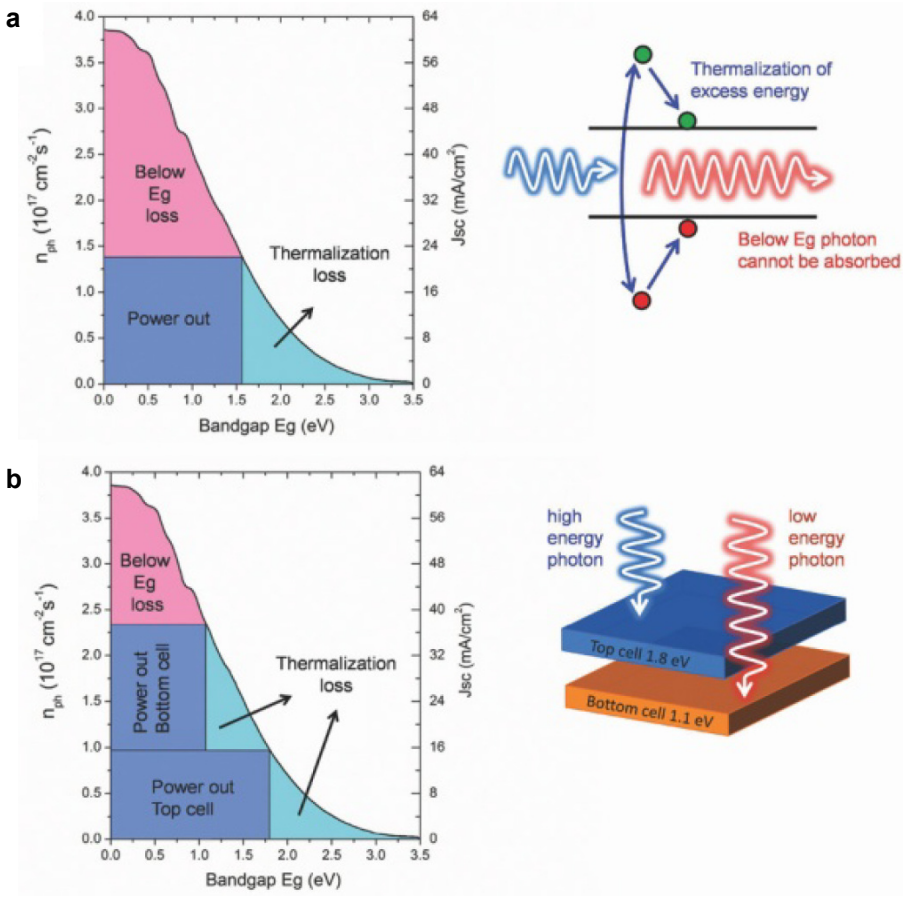


**Figure 6** Schematic diagram of solar spectrum photon energy absorption and loss mechanism of single-junction solar cells (a) and tandem solar cells (b). Reproduced with permission from Ref. [99] ©2017, WILEY-VCH Verlag GmbH & Co. KGaA, Weinheim.

### 3.1.2 *Classification by stacking mode*

Based on the stacking methods of the upper and lower sub-cells, there are two types[102]: mutually independent stacking (Fig. 7a) and tandem integrated stacking (Fig. 7b). The former is relatively straightforward but involves complex manufacturing, resulting in higher costs. In contrast, the latter involves fewer process steps, lower costs, and is promising for high-efficiency. Therefore, it is expected to become the dominant technical approach in the future.

### 3.1.3 *Classification by number of electrode connections*

TSCs can be categorized into three-terminal (3T), four-terminal (4T), and two-terminal (2T) structures based on the number of electrode connections between the upper and lower sub-cells, correspond-

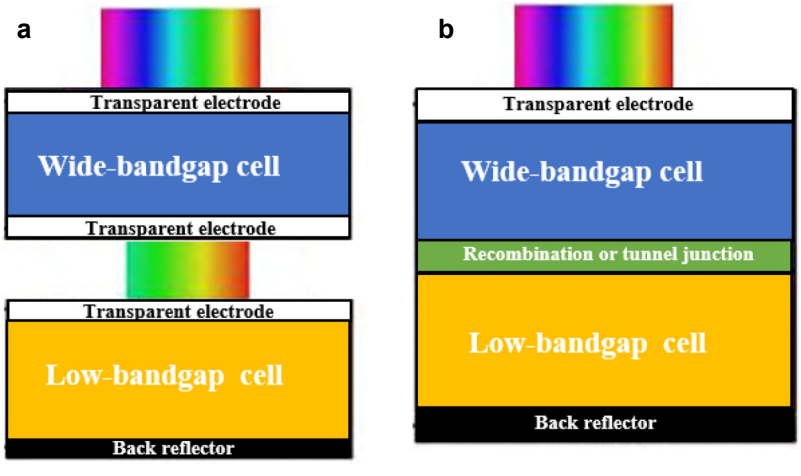


**Figure 7** (a) Stack structure independently of each other. (b) Schematics of tandem integrated structure.

ing to 3, 4, and 2 electrode layers, respectively. In three-terminal TSCs, the top and bottom sub-cells are interconnected via a common intermediate electrode (Fig. 8a), creating a coupled state between them. However, this configuration does not establish an end-to-end connection; thus, the sub-cells are typically connected in parallel for power output. Owing to their operation under high-concentration systems, which results in higher costs, three-terminal TSCs are mainly used in laboratory research and are less common in commercial applications. The four-terminal structure (Figs. 8b–8d) has a relatively straightforward stacking process. In this design, the top and bottom sub-cells are prepared independently and then stacked with an insulating layer in between. This method avoids the need to address compatibility issues or short-circuit current ($I_{sc}$) matching between the sub-cells, resulting in more extensive research and applications for four-terminal structures. For practical use, the two sub-cells in a four-terminal setup are usually connected separately to external loads for power delivery. However, connecting them in series or parallel to form a single entity for power transmission can lead to energy losses, making it less optimal for practical applications. There are three subcategories of four-terminal structure TSCs. (1) Mechanically stacked type (Fig. 8b): This design requires three out of the four electrodes to be transparent. The manufacturing process is complex and costly, often leading to considerable reflection losses and parasitic absorption. (2) Spectrally separated type (Fig. 8c): This structure uses dichroic mirrors to reflect light from the top cell to the bottom cell. However, optical components such as dichroic mirrors are typically expensive, which increases the overall manufacturing cost of this type of four-terminal TSC. Consequently, it is not suitable for large-scale applications. (3) Reflective structure type (Fig. 8d): This design arranges solar cells in a curved pattern to reflect the remaining sunlight onto the focus of the solar converter. It can convert both direct and a portion of diffuse light into electricity. However, the requirement for a curved arrangement makes it suitable only for flexible substrate-based solar cell devices, limiting its application in large-scale photovoltaic power plants. Overall, regardless of the type, four-terminal structures generally involve complex and costly preparation processes.

For two-terminal structure TSCs, which involve tandem integrated stacking (Fig. 8e), the perovskite film is grown directly on the surface of the bottom cell, with the two sub-cells connected in series via a composite layer or a tunnel junction. These TSCs must address process compatibility and current matching ($I_{sc}$) between the two sub-cells. However, compared to four-terminal structure TSCs, two-terminal structure TSCs require only two electrodes (with the upper electrode needing to be transparent). This simplifies the process, reduces manufacturing

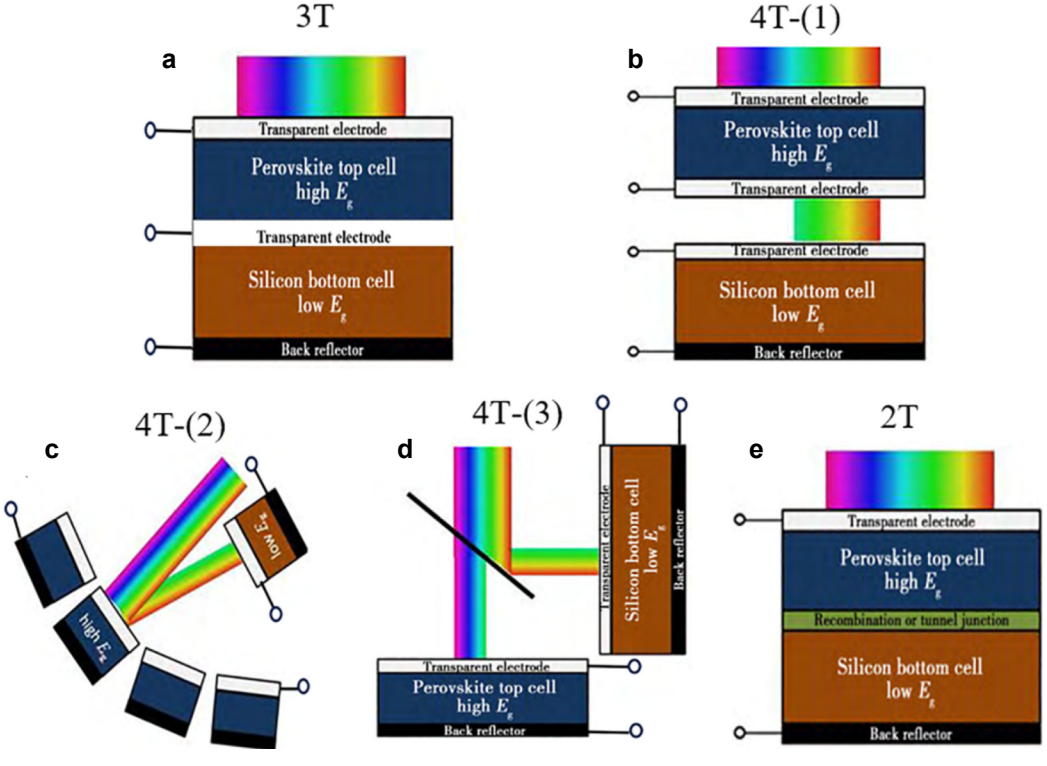


**Figure 8** Structure diagrams of perovskite/crystalline silicon tandem solar cells: three-terminal structure (a), four-terminal mechanically stacked (b), tour-terminal optical spectral splitting (c), four-terminal reflective tandem (d), two-terminal structure (e).

costs, and minimizes parasitic absorption and reflection losses. Given their advantages in processing, cost, and PCE, two-terminal structure TSCs have considerable potential for future development[103,104]. Considering the various classifications discussed, this section will focus on tandem integrated two-terminal structure perovskite/c-Si TSCs.

## 3.2 Key factors affecting the PCE of two-terminal structure perovskite/c-Si TSCs

This section primarily addresses three critical factors influencing the PCE of two-terminal perovskite/c-Si TSCs: optical management, the intermediate interconnecting layer, and $I_{sc}$ matching.

### *3.2.1 Optical management control*

During illumination, two-terminal perovskite/c-Si TSCs experience multiple optical losses owing to refractive index mismatches between different material layers. Reflection loss and parasitic absorption are particularly critical, severely limiting the device's PCE. Thus, effective optical management and regulation are essential.

(1) Reflection loss management

There are typically two approaches to addressing reflection loss. The first is to apply an antireflection layer (such as LiF, $MgF_2$, or polydimethylsiloxane) to the front surface of the TSCs to reduce light reflection[105–107]. The second approach involves using c-Si bottom cells with a light-trapping structure, such as a pyramid structure, to minimize reflection loss and enhance photon capture[108,109]. However, the uneven and rough pyramid structure on the c-Si solar cell surface presents challenges for preparing the perovskite film on top. Solution-processed perovskite films often struggle to maintain their shape on these textured surfaces, requiring a thicker film to ensure complete coverage of the silicon substrate (Fig. 9a)[110]. Perovskite films prepared using two-step evaporation or co-evaporation methods can achieve conformal growth, which helps to minimize reflection loss and consequently reduces current loss (Fig. 9b)[111]. Additionally, using transparent conductive oxides (TCOs) as the interconnect layer in two-terminal perovskite/c-Si TSCs is generally not recommended owing to the refractive index mismatch between TCO and c-Si solar cells, which leads to reflection loss. Instead, employing a hydrogenated nanocrystalline silicon (nc-Si:H) tunnel junction can effectively mitigate this reflection loss.

Previous literature on two-terminal perovskite/c-Si TSCs reveals considerable advancements. Jošt et al.[106] used textured optical management foils on the front, as shown in Fig. 10a, which increased the device's PCE from 23.4% to 25.5%. Tockhorn et al.[112] introduced a 110 nm-thick nc-Si:H layer with a refractive index of 2.6 between the TCO and the c-Si passivation layer, depicted in Fig. 10b. This addition considerably reduced infrared reflection losses and led to a 1.4 mA/cm² increase in $I_{sc}$ for the c-Si bottom cell. Consequently, the 1 cm² two-terminal structure perovskite/c-Si TSCs achieved a $J_{sc}$ of up to 38.7 mA/cm², with a certified steady-state PCE of 25.2%.

**(2) Parasitic absorption management**

In the two-terminal structure perovskite/c-Si TSCs, both the perovskite and c-Si layers act as light absorbers, converting photon energy into photocurrent. However, other functional layers can lead to parasitic absorption. This type of absorption not only fails to contribute to the photocurrent but also results in the loss of incident photon energy. Parasitic absorption commonly occurs in layers such as the TCO, which is used as an electrode, metal oxide films that act as buffer layers, and fullerene $C_{60}$ in PIN-type two-terminal structure perovskite/c-Si TSCs. The photoelectrons and photoholes generated in these layers may recombine with photocarriers in the light-absorbing layer instead of being transferred to the external circuit to produce current. Owing to internal energy losses from recombination processes, some of the absorbed photon energy is dissipated as

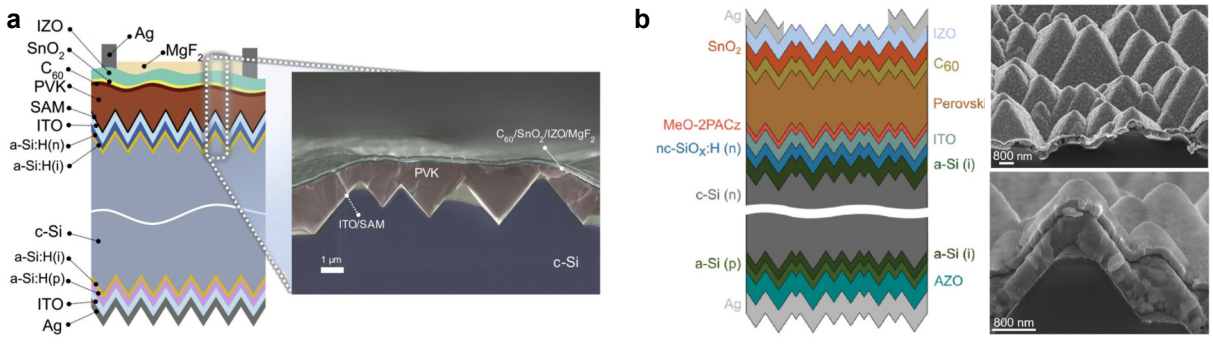


**Figure 9** (a) Structure diagram and SEM image of two-terminal perovskite/crystalline silicon tandem solar cells prepared by solution method (scraping). Reproduced with permission from Ref. [110] ©2021, Elsevier Inc. (b) Structure diagram and SEM image of two-terminal perovskite/crystalline silicon tandem solar cells prepared by a two-step process of evaporating solution. Reproduced under the CC BY license from Ref. [111] ©2021, The Authors.

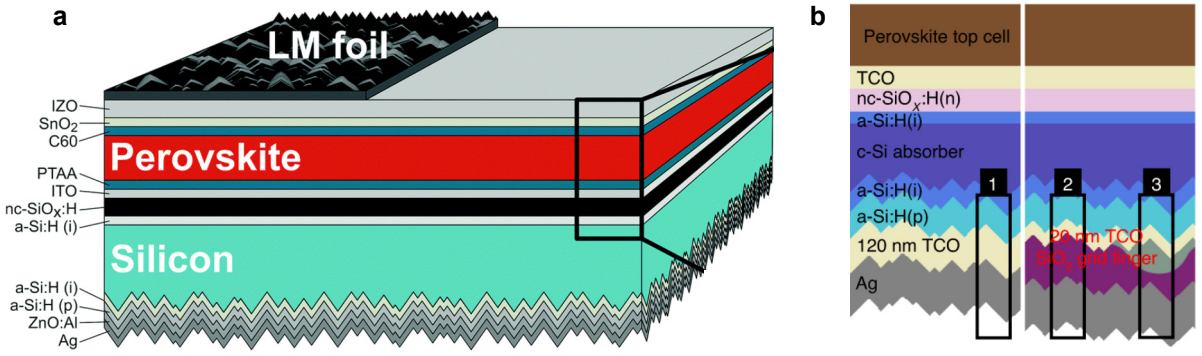


**Figure 10** (a) Structure diagram of tandem solar cells using reduced foil. Reproduced under the CC BY-NC license from Ref. [106] ©2018, The Authors. (b) Structure diagram of tandem solar cells using nanocrystalline silicon oxide antireflection layer. Reproduced under the CC BY 4.0 license from Ref. [112] ©2022, The Authors.

heat, leading to decreased device PCE. To mitigate parasitic absorption caused by TCO, strategies include thinning the TCO film or substituting it with electrodes that have lower carrier concentration and higher carrier mobility, such as indium hydroxide (IO:H) or zirconium-doped indium oxide (IZrO)[113–115]. For parasitic absorption in buffer and carrier transport layers, reducing their thickness or exploring alternative materials with lower parasitic absorption can be effective. Additionally, using appropriate tunnel junctions instead of TCO for the intermediate interconnecting layer in two-terminal perovskite/c-Si TSCs can further minimize parasitic absorption losses.

### 3.2.2 *Intermediate interconnecting layer*

The four-terminal structure TSCs do not require an intermediate interconnection layer. In contrast, two-terminal structure TSCs require this layer to fulfill both optical transmission and electrical connection requirements, which are crucial for achieving high PCE. First, the intermediate interconnection layer must exhibit high optical transparency, with minimal parasitic light absorption and reflection in the long-wave band. Second, it must provide effective electrical connectivity between the two sub-cells, ensuring that photogenerated electrons and holes are recombined at the contact interface with minimal resistance loss. In two-terminal structure TSCs, if the configuration is PIN/PN type, the contact interface between the sub-cells recombines photogenerated electrons from the top cell with photogenerated holes from the bottom cell. Conversely, in an NIP/NP-type structure, the interface recombines photogenerated holes from the top cell with photogenerated electrons from the bottom cell. The recombination process is crucial for eliminating the parasitic potential barrier (reverse electric field) at the contact interface. Inadequate recombination can lead to the accumulation of photogenerated charges at the interface, disrupting the built-in electric field of the solar cell and reducing its performance. Overall, the design of the intermediate interconnection layer adheres to two primary principles. First, as the window layer for the bottom cell, it should minimize optical parasitic absorption and reflection in the visible-near infrared spectrum to maximize the spectral utilization of the bottom cell. Second, as the connection layer between the sub-cells, it must possess high conductivity to facilitate the recombination of opposite charges at the upper and lower interfaces and to reduce the voltage drop at the interface[116,117].

Currently, there are two main types of materials used for intermediate interconnect layers. One type is ultra-thin metal composite layers, primarily made from TCOs such as indium tin oxide (ITO), indium-doped zinc oxide (IZO), zinc-doped tin oxide (ZTO), aluminum-doped zinc oxide (AZO), and IZrO. The other type consists of tunnel junction materials, which can be either homogeneous or heterogeneous, such as heavily doped n++/p++ silicon series.

**(1) TCO composite layer materials**

In 2016, Werner et al.[118] developed IZO transparent composite layers to connect the top and bottom sub-cells in two-terminal perovskite/c-Si TSCs (Fig. 11a). By optimizing the thickness of each layer and the preparation process of the perovskite absorption layer, the device demonstrated stable performance and minimal hysteresis. The 0.17 $cm^2$ device achieved a PCE of 21.2%, while the 1.22 $cm^2$ device achieved a PCE of 19% (Fig. 11b). The researchers later used roughened silicon for the bottom cell to improve near-infrared spectral response, resulting in a 1.43 $cm^2$ two-terminal perovskite/c-Si TSC with a PCE of 20.5%. Ashouri et al.[119] investigated two-terminal perovskite/c-Si TSCs using ITO composite layers (Fig. 11c) and achieved a PCE exceeding 25%.

ITO is commonly used in two-terminal structure TSCs with a PCE greater than 25% owing to its high electrical conductivity and light transmittance[112,120,121]. However, the high lateral electrical conductivity of ITO can lead to local leakage and voltage loss if selective charge transfer layers in the top cell are unevenly deposited. To address this, the conductivity and work

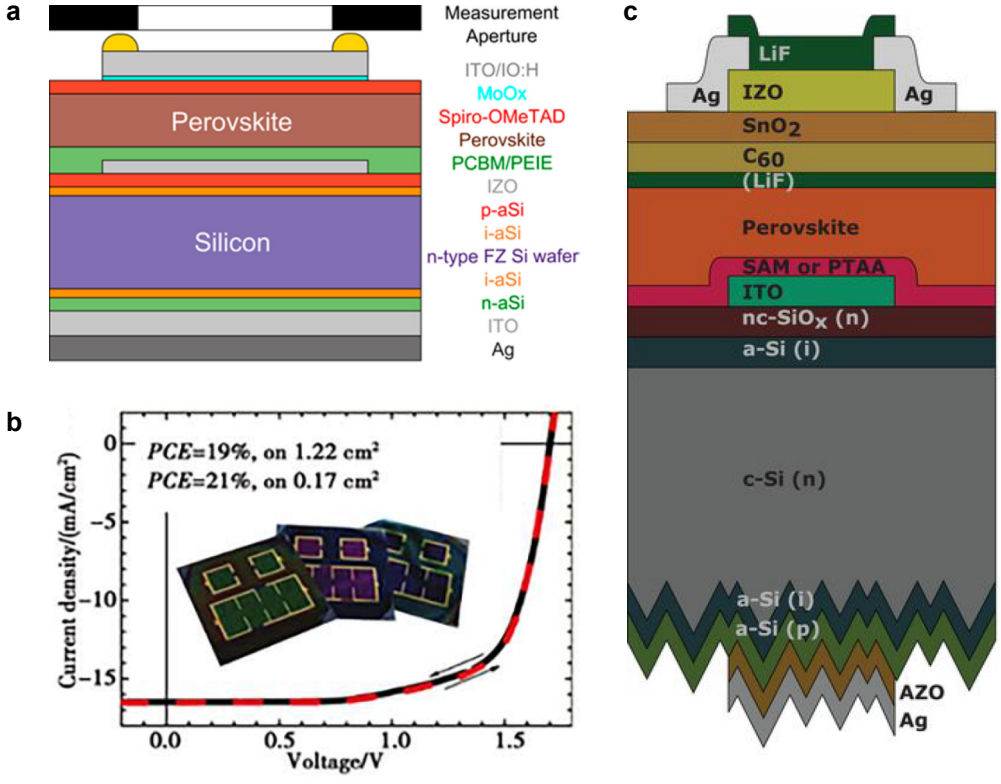


**Figure 11** Structure diagram (a) and *J*–*V* curve (b) of ITO/IOH front electrode perovskite/crystalline silicon tandem solar cells. Reproduced with permission from Ref. [118] ©2015, American Chemical Society. (c) Structure diagram of perovskite/crystalline silicon tandem solar cells with ITO as a composite layer. Reproduced with permission from Ref. [119] ©2020, The Authors.

function of ITO can be optimized by adjusting its doping concentration. Additionally, using a smooth bottom cell surface and ensuring more uniform deposition processes for the top cell can enhance performance. Balancing high electrical conductivity with high visible light transmittance remains a challenge. Typically, ITO is replaced by IZO, which offers higher carrier mobility, to ensure both high conductivity and improved solar light transmittance[122]. However, challenges remain regardless of the type of TCO material used for the intermediate interconnecting layer in two-terminal perovskite/c-Si TSCs. For instance, the refractive index mismatch between the TCO and the bottom c-Si cells leads to light reflection losses above 800 nm. Additionally, the high lateral conductivity of TCO can exacerbate shunting in the top cell, which impedes the efficiency of large-area TSCs. To address these issues, thin semi-transparent metal electrodes can be considered as alternatives to TCO. Uzum et al.[123] used Ag nanoelectrodes as an intermediate interconnecting layer to connect a perovskite top cell with Au electrodes to a c-Si bottom cell. Their two-terminal perovskite/c-Si TSCs exhibited an increase in $J_{sc}$ from 5.4 to 6.93 mA/cm$^2$, and the PCE improved by 0.5% compared to devices with direct Au electrode connections to the c-Si cell. Despite this improvement, the PCE remained relatively low, indicating that further enhancements in the quality of the intermediate interconnecting layer was required to enhance device performance.

**(2) Tunnel junction layer materials**

Commonly used Si-based n++/p++ tunnel junction layer materials in two-terminal perovskite/c-Si TSCs include amorphous silicon (a-Si) and nc-Si:H. Both materials exhibit favorable properties such as low lateral conductivity, minimal parasitic absorption, and reduced reflection loss, making them ideal for tunnel junction layers. For example, nc-Si:H has lower parasitic absorption in the visible light range, and its grain boundaries contribute to considerably increased lateral resistivity. This helps to reduce the risk of lateral leakage from the top cell. The doping concentration can be adjusted to lower the tunneling barrier and improve tunneling properties by depositing tunnel junction films using plasma enhanced chemical vapor deposition (PECVD). As shown in Fig. 12[124], effective charge transfer with minimal $V_{oc}$ loss can be achieved through either single tunneling or multistep trap-assisted tunneling.

In 2015, n++ a-Si was introduced as a tunnel junction layer on the emitter of p++ Si[125]. The experimental results demonstrated that the p++/n++ hydrogenated a-Si (a-Si:H) effectively facilitated the recombination of photogenerated electrons in the top cell and photogenerated holes in the c-Si bottom cell. The two-terminal perovskite/c-Si TSCs achieved a PCE of 13.7% and a $V_{oc}$ of 1.58 V, marking the first successful application of a tunnel junction as an

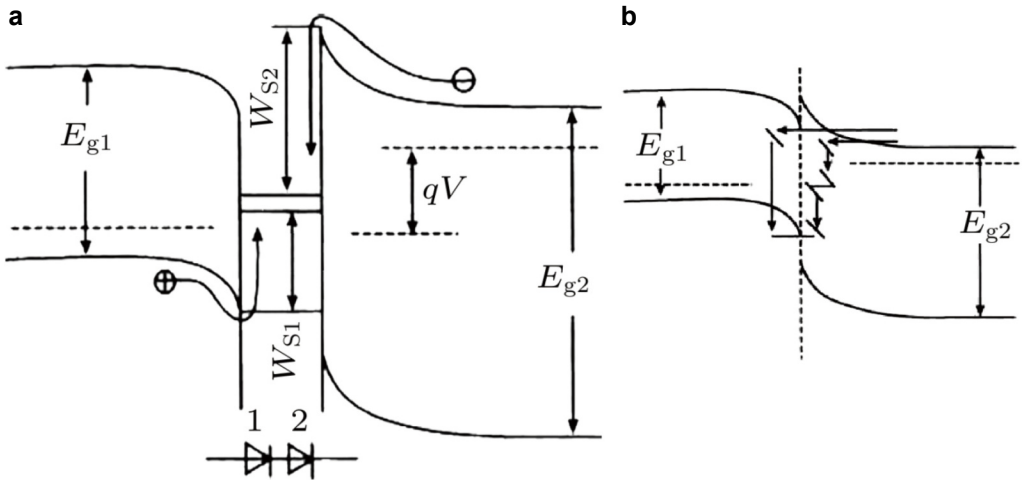


**Figure 12** (a) Interface composite model. (b) Tunnel composite model. Reproduced with permission from Ref. [124] ©2023, Chinese Physical Society.

interconnect layer in such devices. However, the fabrication of this tunnel junction layer requires high-temperature annealing at 680 °C, which is not compatible with heterojunction (HJT) bottom cells. Therefore, developing a low-temperature method for preparing tunnel junction layer materials compatible with HJT bottom cells is essential. In 2017, Sahli et al.[126] developed an n++/p++ nc-Si:H film using PECVD at temperatures below 200 °C for use as a tunnel junction layer in two-terminal perovskite/HJT c-Si TSCs. The HTL material Spiro-TTB effectively covered the nc-Si:H layer. Additionally, the high-density grain boundaries in the nc-Si tunnel junction layer helped prevent lateral carrier transport, reducing leakage and shunt effects in the top cell. With optimized perovskite layer composition, the device achieved a certified steady-state PCE of 25.2%. They further used the low-temperature PECVD-prepared p++/n++ nc-Si:H tunnel junction layer in perovskite/HJT c-Si devices (Fig. 13a) and also analyzed the optical advantages of nc-Si:H compared to ITO. First, the bandgap of the p++/n++ nc-Si:H tunnel junction layer is considerably smaller than that of ITO (Fig. 13b), absorbing only the blue spectrum region and thus having minimal negative impact on the overall performance of the TSCs. Second, the nc-Si:H tunnel junction layer exhibits slightly lower light absorption in the near-infrared region (>800 nm) compared to ITO. Third, the refractive index of nc-Si:H closely matches that of c-Si (3.6–3.7@800 nm), leading to reduced reflectivity in the 700–900 and 1000 nm regions (Fig. 13c). This allows more photons to be absorbed by the bottom cell. Consequently, the nc-Si:H tunnel junction layer minimizes light reflection at the sub-cell interface and enhances light transmission to the bottom cell. Given the advantages of low lateral conductivity and low-temperature processing associated with this tunnel junction layer, this method is likely to become the mainstream approach for preparing large-scale interconnecting layers in two-terminal perovskite/c-Si TSCs in the future.

Additionally, the doping concentration impacts the tunneling effect of silicon tunnel junction materials, which in turn affects the recombination of photogenerated carriers at the interconnecting interface. Rolland et al.[127] used Atlas software (Silvaco Group, Inc.) to simulate the effects of varying tunnel junction doping concentrations on the performance of two-terminal perovskite/c-Si TSCs. They discovered that an effective tunneling effect is achieved with the lowest doping concentrations of n++ and p++ at $5 \times 10^{19}$ $cm^{-3}$, which facilitates effective interconnection between the two sub-cells. With further optimization, the device achieved a PCE of 27%.

### 3.2.3 *$I_{sc}$ matching*

For three-terminal or four-terminal structure TSCs, matching the $I_{sc}$ of the top and bottom sub-cells is not required. However, for two-terminal structure TSCs, $I_{sc}$ matching is crucial because the top and bottom sub-cells are connected in series. Theoretically, in two-terminal structure TSCs, the total $V_{oc}$ is the sum of the $V_{oc}$ of the top cell and the $V_{oc}$ of the bottom cell, while the total $I_{sc}$ is determined by the smaller of the two values. This occurs because, in a series circuit, there is only one path for current flow, ensuring that the current is uniform throughout the circuit. The sub-cell with the smaller $I_{sc}$ typically indicates a material with a wider bandgap. As a result, fewer electrons can be excited under illumination, leading to a lower carrier concentration. According to the resistivity formula, this lower carrier concentration results in higher resistivity and increased internal resistance. Consequently, the sub-cell with lower $I_{sc}$ generates a higher photovoltage, while the other sub-cell generates less, which ultimately reduces the photocurrent of the entire series

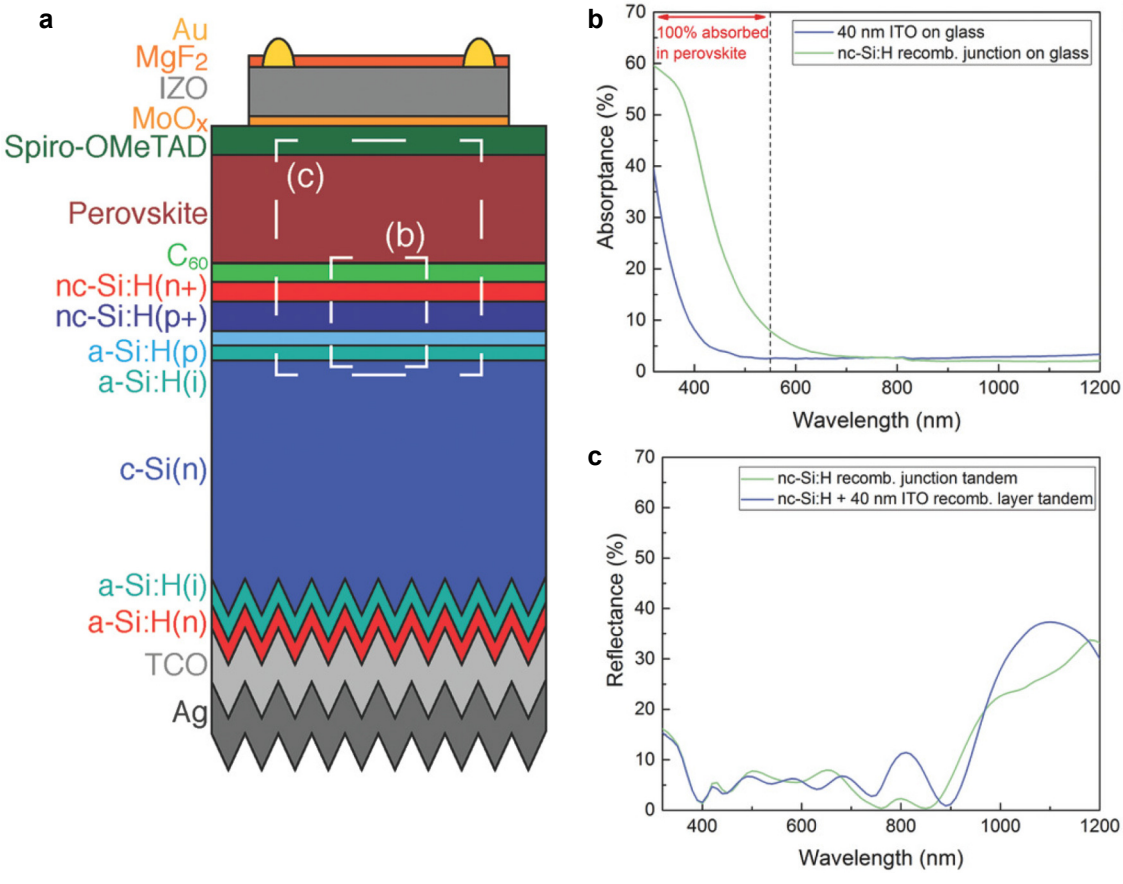


**Figure 13** (a) Schematic diagram of perovskite/SHJ tandem solar cells. (b) Absorptance of ITO/glass and nc-Si:H/glass. (c) Reflectance of tandem solar cells with different interconnect layer. Reproduced with permission from Ref. [126] ©2017, WILEY-VCH Verlag GmbH & Co. KGaA, Weinheim.

circuit. Therefore, achieving optimal $I_{sc}$ matching between the top and bottom sub-cells is crucial for two-terminal structure TSCs to avoid the described mismatch effect and to attain higher PCE. In two-terminal perovskite/c-Si TSCs, the bandgap of c-Si is 1.12 eV, which is considered when striving for ideal $I_{sc}$ matching between the sub-cells. One requirement is that the perovskite top cell should effectively absorb photon energy from ultraviolet and visible light in the range of 300–750 nm. Another requirement is that it should not absorb photon energy in the longer wavelength spectra. Achieving this involves selecting a perovskite material with a bandgap in the range of 1.67–1.75 eV. However, wide-bandgap perovskites often face considerable issues with non-radiative recombination losses and unresolved stability problems. Similar to single-junction narrow-bandgap PSC, the non-radiative recombination losses in wide-bandgap perovskite top cells in TSCs can be mitigated through additive engineering. Chen et al.[128] enhanced device performance by incorporating $MAH_2PO_2$ and MACl into the perovskite precursor, which reduced the density of grain boundary states and, consequently, minimized non-radiative recombination. Xu et al.[129] introduced Cl doping into the perovskite sample, effectively passivating interface defects and thereby improving the photogenerated minority carrier lifetime and mobility. This reduction in defect-related $V_{oc}$ loss decreased from over 0.5 V to approximately 0.45 V, resulting in a PCE of 20.42%, with $J_{sc}$ of 20.18 mA/cm$^2$, $V_{oc}$ of 1.217 V, and FF of 0.83. Notably, phase separation was considerably suppressed under 100 times the standard sunlight intensity. After 1000 h of maximum power point tracking (MPPT), the top cell's PCE degradation was less than 4%. Figures 14a and 14b show the schematic diagram and cross-sectional SEM image of the two-terminal structure perovskite/c-Si (polished front surface) TSCs. The device, with an effective area of 1 cm$^2$, achieved a PCE of 27.13% ($J_{sc}$ = 19.12 mA/cm$^2$, $V_{oc}$ = 1.886 V, FF = 0.75), as shown in Fig. 14c. The external quantum efficiency of the bottom c-Si cell is low in the 800–900 nm wavelength range, as shown in Fig. 14d, owing to interface reflection between the two sub-cells. It is expected that using a double-sided velvet HJT bottom cell could increase $J_{sc}$ to over 20 mA/cm$^2$.

In 2018, Qiu et al.[130] achieved $I_{sc}$ matching between the top and bottom sub-cells by optimizing the performance of the ETL and by adjusting the bandgap and thickness of the perovskite. The PCE of

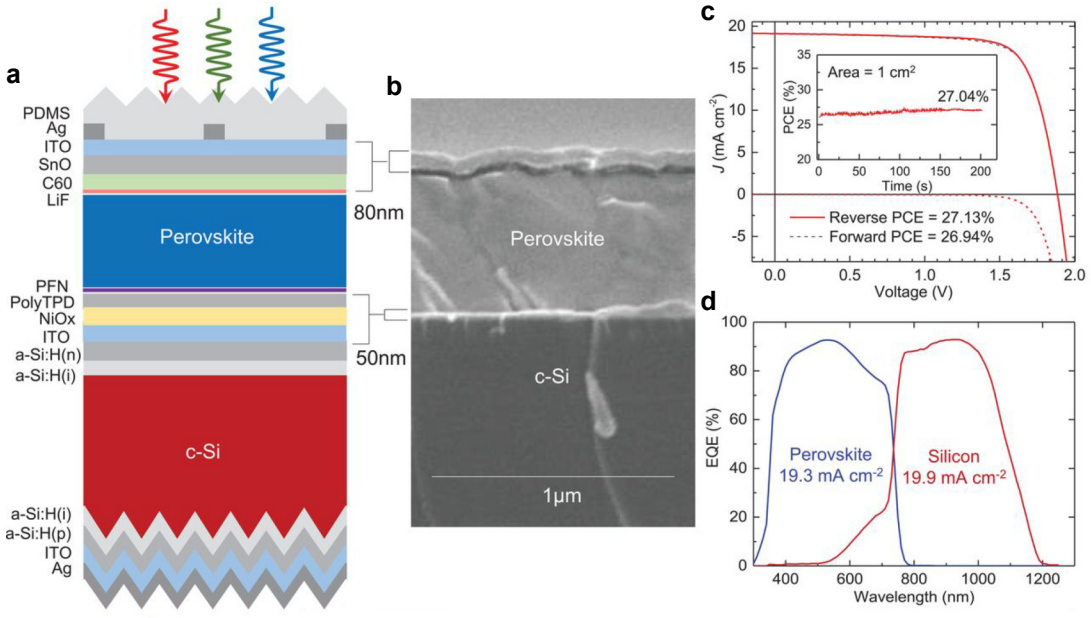


**Figure 14** (a) Schematic of the two-terminal structure perovskite/crystalline silicon tandem solar cells (not to scale). (b) Cross-sectional SEM image. (c) Light and dark *J*–*V* curves and MPPT (inset) of the champion tandem. (d) EQE spectra of the champion tandem. Reproduced with permission from Ref. [129] ©2020, The Authors.

the two-terminal structure TSCs, based on a perovskite with a 1.69 eV bandgap and c-Si, reached 22.22%. That same year, Zhu et al.[131] systematically investigated the impact of different solvents on the surface structure of perovskite materials and the performance of two-terminal structure TSCs. By optimizing the solvent in the perovskite precursor solution, the researchers improved the quality of the perovskite film and achieved a better balance between perovskite light absorption and transmittance. Additionally, excellent current matching was achieved, and the device stability was improved. Kim et al.[132] achieved $I_{sc}$ matching by modifying the bandgap and thickness of the perovskite and using PTAA as the HTL to adjust the band alignment. Their final device achieved a PCE of 21.19%.

### 3.3 Research status of all-inorganic perovskite/c-Si TSCs

Currently, all types of perovskite/c-Si TSCs in experimental research and commercial applications primarily use organic–inorganic hybrid perovskites for the top cell, including two-terminal, three-terminal, and four-terminal structures. However, there are few examples of perovskite/c-Si TSCs with all-inorganic perovskite top cells, and existing literature predominantly focuses on simulation studies. In 2021, Islam et al.[133] investigated the performance of two-terminal structure perovskite/c-Si TSCs using $CsSn_{0.5}Ge_{0.5}I_3$ and $MAPbI_3$ as the top cells, employing SCAPS simulation software. They determined the optimal thicknesses for $CsSn_{0.5}Ge_{0.5}I_3$ and $MAPbI_3$ to be 365 nm and 225 nm, respectively. The two-terminal structure $CsSn_{0.5}Ge_{0.5}I_3$/c-Si TSCs achieved a PCE of 28.53%. This study demonstrated the feasibility of fabricating high-efficiency two-terminal structure $CsSn_{0.5}Ge_{0.5}I_3$/c-Si TSCs. In the same year, Azadinia et al.[134] investigated maximum single-junction and lead-free all-inorganic perovskite TSCs, using $CsSnI_3$ and $CsGeI_3$ sub-cells in series with c-Si sub-cells. They also evaluated the performance of $CsSn_xGe_{1-x}I_3$ solar cells. In 2022, Jayan et al.[135] used SCAPS-1D simulation software to explore the photovoltaic performance and optimization parameters of $CsPbI_3$/c-Si TSCs with both two-terminal and four-terminal structures. They used IGZO and $CuSbS_2$ as the ETL and HTL for the top cell, respectively. Optimal performance of the TSCs was achieved by adjusting the thickness, dopant density, and defect density of $CsPbI_3$ and c-Si to meet the $I_{sc}$ matching conditions. For the two-terminal structure TSCs, with $CsPbI_3$ and c-Si layers of 1100 nm- and 6.9 μm-thicknesses, respectively, the PCE reached 27.07%. In contrast, the four-terminal structure TSCs achieved a PCE of 30.68%.

Subsequently, Hossain et al.[136] investigated highly efficient two-terminal structure TSCs consisting of $CsPbI_2Br$ and a-si:H/c-Si using SCAPS-1D simulation software, as depicted in Fig. 15. They first calibrated the two independent sub-cells to match experimental results reported in the literature, then evaluated the performance of the designed TSCs. Using a 0.5 μm $CsPbI_2Br$ film for the top cell and adjusting the thickness of the bottom c-Si to achieve $I_{sc}$ matching between the two sub-cells, they first improved the PCE of the TSCs to 26.25%. They further enhanced the performance of the top cell by exploring various

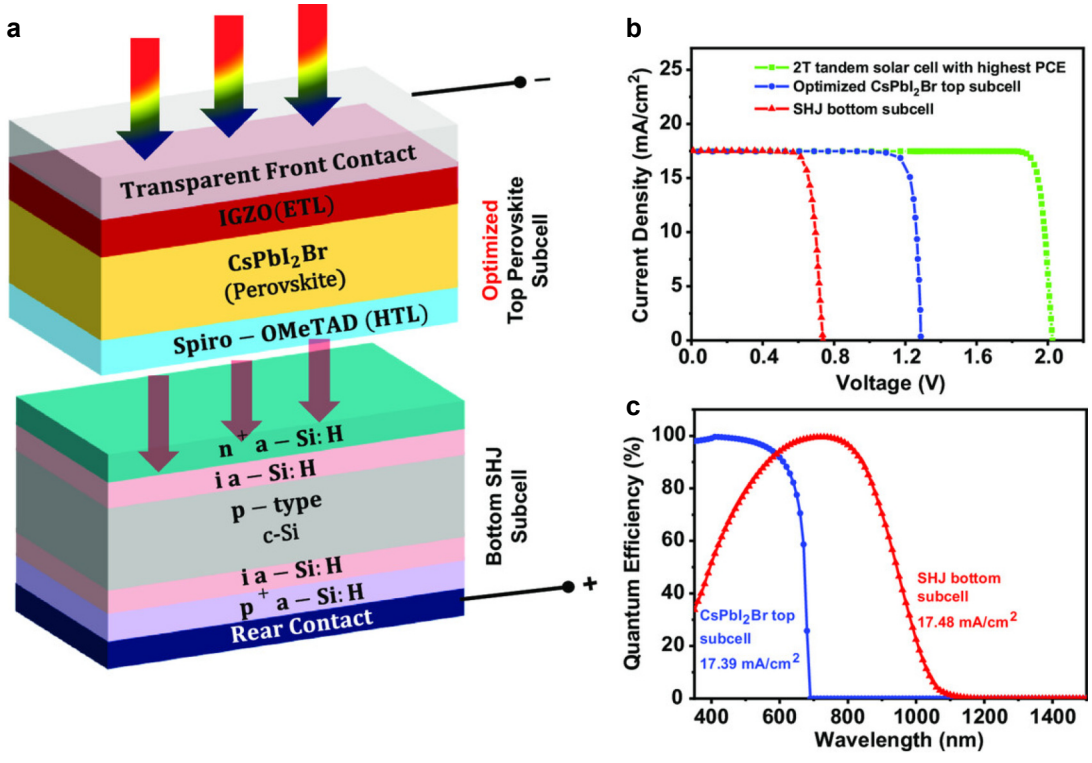


**Figure 15** (a) Schematic diagram of the two-terminal structure TSCs with the optimal top cell. (b) *J*–*V* characteristics of the optimized top cell, bottom cell and two-terminal structure TSCs. (c) Quantum efficiency of the optimized two-terminal structure TSCs. Reproduced with permission from Ref. [136] ©2023, Wiley-VCH GmbH.

ETL and HTL materials and adjusting the work functions of the precontact electrodes. With the front contact work function set to 4 eV, using indium gallium zinc oxide (IGZO) as the ETL and Spiro-OMeTAD as the HTL, the two-terminal TSCs achieved a maximum PCE of 32.44%. These simulation results offer valuable guidance for achieving highly stable and efficient all-inorganic perovskite/c-Si TSCs.

In 2022, Wang et al.[137] performed experimental research on two-terminal TSCs using $CsPbI_xBr_{3-x}$/c-Si (Fig. 16). For the top cell, they implemented an effective strategy using nickel iodide to passivate iodine vacancies and reduce non-radiative recombination. They also alleviated charge accumulation at the perovskite/Spiro-OMeTAD interface by optimizing energy level alignment. The resulting TSCs achieved a PCE of 22.95% and a $V_{oc}$ of 2.04 V. Importantly, these TSCs exhibited excellent operational stability, retaining 95.7% of their initial PCE after 300 h of continuous illumination in a nitrogen atmosphere. This study offers a promising approach for fabricating highly efficient and stable all-inorganic perovskite TSCs with inorganic passivation materials, which can advance their commercialization.

In 2023, Wang et al.[138] continued their research on all-inorganic perovskite/c-Si TSCs with a relevant

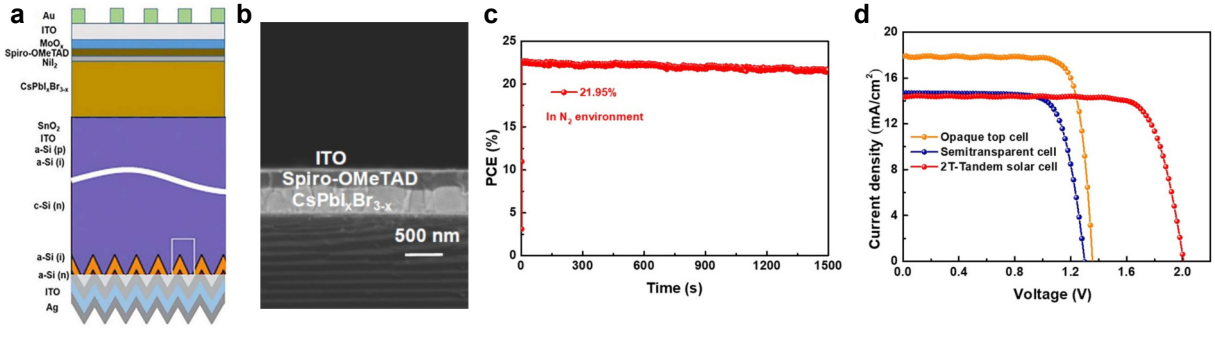


**Figure 16** (a) Schematic diagram of the two-terminal structure $CsPbI_xBr_{3-x}$/c-Si TSCs. (b) SEM cross-section view of the two-terminal structure $CsPbI_xBr_{3-x}$/c-Si TSCs. (c) *J*–*V* characteristics of opaque top cell, semi-transparent top cell, and the two-terminal structure TSCs. (d) Two-terminal structure $CsPbI_xBr_{3-x}$/c-Si TSCs treated in a nitrogen dioxide environment achieved a steady-state efficiency of 21.95% during MPPT of 1500s. Reproduced under the CC BY license from Ref. [137] ©2022, The Authors.

two-terminal structure (Fig. 17). For the $CsPbI_{2.85}Br_{0.15}$ top cell, they developed a method to enhance efficiency by modifying the surface properties of thin films using 2-amino-5-bromobenzamide (ABA). This approach not only facilitated synergistic coordination between the carbonyl (C=O) and amino ($NH_2$) groups with non-coordinated $Pb^{2+}$ but also addressed bromine vacancies, thereby inhibiting the formation of PbO. These processes effectively passivated defects on the top surface, thereby enhancing both the performance and stability of the TSCs. Ultimately, they achieved a PCE of 25.31% for the PIN-type all-inorganic perovskite/c-Si TSCs. Additionally, the TSCs maintained 92.59% of their initial PCE after 200 h of continuous illumination in ambient air, even without encapsulation. This research offers a promising approach for developing highly stable two-terminal all-inorganic perovskite/c-Si TSCs.

## 4 Conclusion and outlook

All-inorganic perovskites and their TSCs with c-Si demonstrate remarkable stability over extended periods, remaining intact under thermal, oxygen, and humidity conditions, while also exhibiting considerable photovoltaic potential. Consequently, their advantages are clear. This review systematically and thoroughly examined the recent advancements in lead-based and tin-based all-inorganic perovskites, along with their associated TSCs. It identifies key challenges and offers recommendations for future research in these areas.

First, while practical applications have been achieved with lead-based single-junction all-inorganic PSC, their crystal structure stability is generally poor. These materials are prone to phase transitions at room temperature, leading to rapid degradation of the solar cell's PCE when exposed to air, which hinders their large-scale commercial viability. To address this issue, researchers have used various strategies to enhance the stability of $CsPbI_3$, which has a low tolerance factor. These strategies include adding substances such as HI and ABA and introducing 2D layers. Additionally, researchers have investigated more stable crystal structures, including $CsPbI_2Br$ and $CsPbIBr_2$, as well as other lead-based inorganic perovskites with varying compositions, such as $CsPbI_{3-x}Br_x$, $CsPb_xSn_{1-x}I_{3-y}Br_y$, and $CsPbBrI_{2-x}F_x$. For future research on lead-based all-inorganic PSC, several key areas warrant attention. First, it is essential to perform in-depth studies on the driving forces and mechanisms behind perovskite crystal structure phase transitions. Second, research should focus on optimizing the annealing and crystal

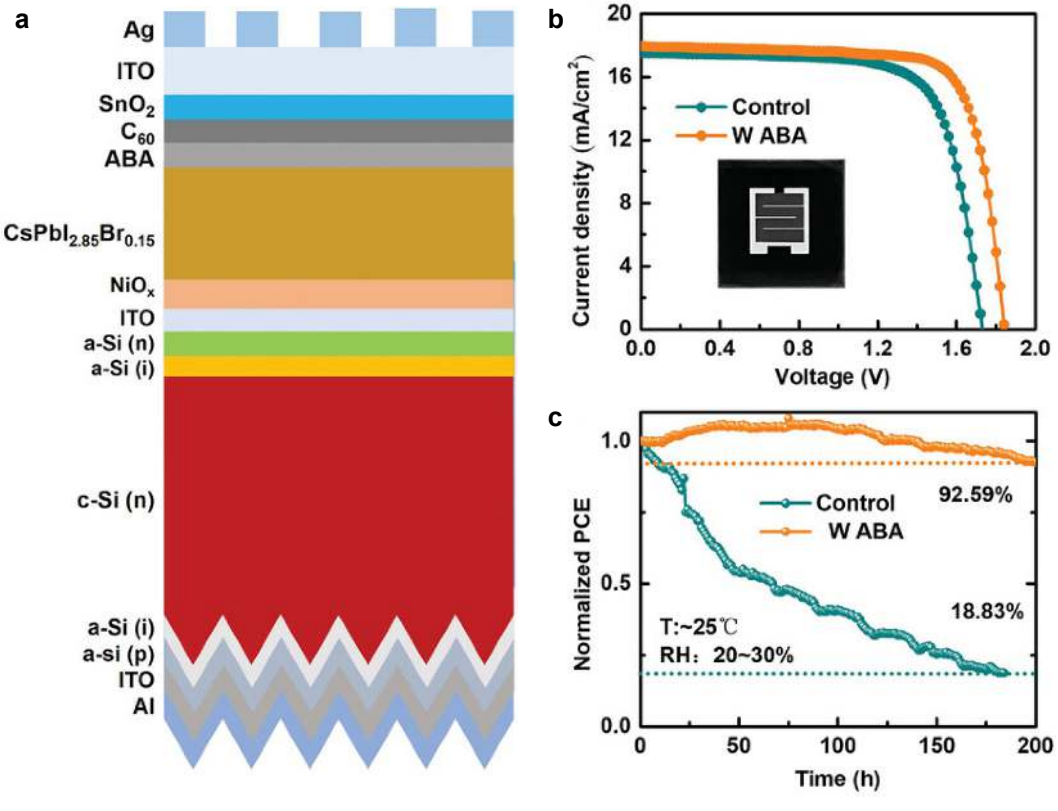


**Figure 17** (a) Schematic diagram of the two-terminal structure $CsPbI_{2.85}Br_{0.15}$/c-Si TSCs. (b) *J*–*V* curves of the champion ABA treated PIN all-inorganic perovskite/c-Si TSCs under one-sun illumination, (c) Operational stability of unencapsulated all-inorganic perovskite/c-Si TSCs under 25% relative humidity, 25 °C, and continuous LED illumination (100 mW/cm²). Reproduced with permission from Ref. [138] ©2023, Wiley-VCH GmbH.

growth processes to achieve large, vertical columnar grain structures. Additionally, scientific theoretical calculations and a comprehensive review of doping theories should be used to guide the targeted doping of metal ions or non-metal halide ions. This approach may enhance the phase stability of lead-based all-inorganic perovskites by improving their tolerance factor. Moreover, further exploration of additives and processes for interface optimization is also necessary. With these research strategies and efforts, it is hoped that future advancements will lead to the development of lead-based all-inorganic perovskites with optimal band gaps, outstanding photoelectric properties, and improved stability, along with enhanced processes for preparing their solar cells.

Second, tin-based single-junction all-inorganic PSC offer a more environmentally friendly core absorption layer and a more suitable bandgap compared to lead-based perovskites. However, their PCE is considerably lower than that of lead-based PSC. This is primarily attributed to the easy oxidation of $Sn^{2+}$ to $Sn^{4+}$ in tin-based perovskites, which creates Sn vacancies and results in p-type doping when exposed to air. This oxidation increases metallicity and dark carrier concentration, while the high dark carrier concentration and strong molecular carrier decay components restrict carrier diffusion and extraction. These issues ultimately affect the PCE of tin-based all-inorganic PSC, which is a considerable challenge for this type of perovskite. Currently, research on single-junction tin-based PSC is less extensive compared to lead-based perovskites. However, several tin-based perovskite materials with improved stability have been identified, such as $Cs_2SnI_6$, $CsSnI_xBr_{3-x}$, and $Cs_2SnI_xBr_{6-x}$ with varying $x$ values. For future research, it is crucial to address the problems of excessive self-doping and high film defect density caused by the oxidation of $Sn^{2+}$ in tin-based perovskites. This can be accomplished by adjusting post-treatment temperatures, introducing functional additives, doping with elements, and passivating interfaces, among other strategies. Continued exploration of alternative perovskite variants is also important. The goal is to develop tin-based all-inorganic perovskites with optimal band gaps, outstanding photoelectric properties, and enhanced stability, along with effective solar cell fabrication processes.

Moreover, research on perovskite-related solar cells reveals that TSCs with multiple junctions are considerably less common than those with a single-junction. Most existing literature focuses on lead-based organic–inorganic hybrid four-terminal TSCs, including configurations such as lead-inorganic perovskite/lead–hybrid perovskite and lead–hybrid perovskite/c-Si four-terminal TSCs. In terms of commercial applications, the relatively short period of research means that related theories and technologies are still evolving. Consequently, many companies choose organic–inorganic hybrid perovskite materials, which are prone to decomposition under heat, and adopt complex, costly four-terminal structures to achieve high PCE values and attract market investment. Additionally, the charge transport layers in perovskite sub-cells often rely on highly efficient but complex and costly organic materials, such as Spiro-OMeTAD, commonly used as HTLs in high-efficiency TSCs. This approach presents several challenges. First, it does not align with the goals of cost-effectiveness and simplicity. Second, it falls short of meeting long-term durability requirements. According to industry standards, large-scale commercial solar cell modules are expected to have a design life of approximately 25 years, maintaining performance even in harsh outdoor conditions, including exposure to wind, sun, rain, and extreme temperatures, such as those exceeding 70 °C in desert environments. Thus, the use of organic components in critical layers of TSCs—such as perovskite absorption layers or charge transport layers—poses a challenge. These organic materials are prone to aging and decomposition, which can considerably impact the overall stability and lifespan of the device.

In contrast, all-inorganic perovskite/c-Si TSCs, with their entirely inorganic functional layers, offer considerable overall advantages. However, several challenges remain. For instance, in two-terminal structure TSCs, which are seen as highly promising, the $I_{sc}$ is dictated by the sub-cell with the lower current. Therefore, it is crucial to closely match the $I_{sc}$ of both sub-cells to optimize performance. Additionally, the top cell's film is deposited directly onto the c-Si bottom cell, and it is vital that the fabrication process for the top cell's layers does not compromise the performance of the bottom cell. This challenge is particularly pronounced when aiming to achieve high-performance perovskite cells on a textured c-Si bottom cell. Moreover, the tunnel junction in the intermediate interconnection layer requires further in-depth research. Despite some unresolved issues in developing all-inorganic perovskite/c-Si TSCs, their overall advantages are substantial. From a long-term perspective in the photovoltaic industry, these TSCs hold considerable potential and promise. Consequently, future research should focus on exploring superior inorganic perovskite materials and fabrication processes for tandem cells. This includes enhancing the crystallinity of the perovskite absorber layer, minimizing grain boundary and surface defect states, and mitigating ion migration and phase segregation. Developing wide-bandgap top cell technologies with minimal photoelectric losses, along with exceptional inorganic ETL and HTL materials and

their fabrication processes, should be prioritized. This includes enhancing carrier extraction capabilities through modifications in carrier transport layers or doping. Additionally, addressing integration challenges between the top and bottom cells is crucial, such as optimizing energy level alignment, achieving current matching between sub-cells, and improving optical management to minimize reflection losses and parasitic absorption. Exploring high-performance tunnel junction materials with appropriate doping concentrations for the intermediate interconnection layer is also essential. These efforts aim to create all-inorganic perovskite/c-Si TSCs that are environmentally friendly, cost-effective, efficient, durable, and simple to fabricate.

## Acknowledgments

None.

## Author contribution statement

Hongjun Wu: writing-original draft. Zhaorui Sun: formal analysis, investigation. Haonan Li: formal analysis, investigation. Xiuhua Chen: supervision, funding acquisition. Wenhui Ma: supervision. Shaoyuan Li: writing-review & editing. Zhengjie Chen: formal analysis, writing-review & editing. Fengshuo Xi: formal analysis, investigation. All the authors have approved the final manuscript.

## Data availability

Not applicable.

## Declaration of competing interest

All the contributing authors report no conflict of interests in this work.

## Funding

This work is granted by the National Natural Science Foundation of China (Grant Nos. 52164050 and 51762043), Major Science and Technology Project of Yunnan Province (Grant No. 202202AB080010).

## Use of AI statement

None.

## References

[1] Kojima, A., Teshima, K., Shirai, Y., Miyasaka, T. (2009). Organometal halide perovskites as visible-light sensitizers for photovoltaic cells. *J. Am. Chem. Soc.* 131, 6050–6051.

[2] Kim, H. S., Lee, C. R., Im, J. H., Lee, K. B., Moehl, T., Marchioro, A., Moon, S. J., Humphry-Baker, R., Yum, J. H., Moser, J. E., et al. (2012). Lead iodide perovskite sensitized all-solid-state submicron thin film mesoscopic solar cell with efficiency exceeding 9%. *Sci. Rep.* 2, 591.

[3] Liu, Z., Chen, X. L., Hou, G. F., Li, Y. L., Ding, Y., Zhao, Y., Zhang, X. D. (2021). Research progress of high-efficiency perovskite solar cells and their tandem cells (*in Chinese*). *Mater. Rep.* 35, 15031–15046.

[4] Hwang, B., Lee, J. S. (2017). Hybrid organic-inorganic perovskite memory with long-term stability in air. *Sci. Rep.* 7, 673.

[5] Pellegrino, G., Colella, S., Deretzis, I., Condorelli, G. G., Smecca, E., Gigli, G., La Magna, A., Alberti, A. (2015). Texture of $MAPbI_3$ layers assisted by chloride on flat $TiO_2$ substrates. *J. Phys. Chem. C* 119, 19808–19816.

[6] Lee, J. W., Kim, D. H., Kim, H. S., Seo, S. W., Cho, S. M., Park, N. G. (2015). Formamidinium and cesium hybridization for photo- and moisture-stable perovskite solar cell. *Adv. Energy Mater.* 5, 1501310.

[7] Aristidou, N., Sanchez-Molina, I., Chotchuangchutchaval, T., Brown, M., Martinez, L., Rath, T., Haque, S. A. (2015). The role of oxygen in the degradation of methylammonium lead trihalide perovskite photoactive layers. *Angew. Chem. Int. Ed.* 54, 8208–8212.

[8] Boyd, C. C., Cheacharoen, R., Leijtens, T., McGehee, M. D. (2019). Understanding degradation mechanisms and improving stability of perovskite photovoltaics. *Chem. Rev.* 119, 3418–3451.

[9] Xiao, C. X., Li, Z., Guthrey, H., Moseley, J., Yang, Y., Wozny, S., Moutinho, H., To, B., Berry, J. J., Gorman, B., et al. (2015). Mechanisms of electron-beam-induced damage in perovskite thin films revealed by cathodoluminescence spectroscopy. *J. Phys. Chem. C* 119, 26904–26911.

[10] De Roo, J., Ibáñez, M., Geiregat, P., Nedelcu, G., Walravens, W., Maes, J., Martins, J. C., Van Driessche, I., Kovalenko, M. V., Hens, Z. (2016). Highly dynamic ligand binding and light absorption coefficient of cesium lead bromide perovskite nanocrystals. *ACS Nano* 10, 2071–2081.

[11] Richter, A., Hermle, M., Glunz, S. W. (2013). Reassessment of the limiting efficiency for crystalline silicon solar cells. *IEEE J. Photovoltaics* 3, 1184–1191.

[12] Keppner, H., Torres, P., Flückiger, R., Meier, J., Shah, A., Fortmann, C., Fath, P., Willeke, G., Happle, K., Kiess, H. (1994). Passivation properties of amorphous and microcrystalline silicon layers deposited by VHF-GD for crystalline silicon solar cells. *Solar Energy Mater. Solar Cells* 34, 201–209.

[13] Wang, Y. X., Zhao, H. R., Piotrowski, M., Han, X., Ge, Z. S., Dong, L. Z., Wang, C. J., Pinisetty, S. K., Balguri, P. K., Bandela, A. K., et al. (2022). Cesium lead iodide perovskites: optically active crystal phase stability to surface engineering. *Micromachines* 13, 1318.

[14] Travis, W., Glover, E. N. K., Bronstein, H., Scanlon, D. O., Palgrave, R. G. (2016). On the application of the tolerance factor to inorganic and hybrid halide perovskites: a revised system. *Chem. Sci.* 7, 4548–4556.

[15] Steele, J. A., Jin, H. D., Dovgaliuk, I., Berger, R. F.,

Braeckevelt, T., Yuan, H. F., Martin, C., Solano, E., Lejaeghere, K., Rogge, S. M. J., et al. (2019). Thermal unequilibrium of strained black $CsPbI_3$ thin films. *Science* 365, 679–684.

[16] Choi, H., Jeong, J., Kim, H. B., Kim, S., Walker, B., Kim, G. H., Kim, J. Y. (2014). Cesium-doped methylammonium lead iodide perovskite light absorber for hybrid solar cells. *Nano Energy* 7, 80–85.

[17] Eperon, G. E., Paternò, G. M., Sutton, R. J., Zampetti, A., Haghighirad, A. A., Cacialli, F., Snaith, H. J. (2015). Inorganic caesium lead iodide perovskite solar cells. *J. Mater. Chem. A* 3, 19688–19695.

[18] Xiang, S. S., Fu, Z. H., Li, W. P., Wei, Y., Liu, J. M., Liu, H. C., Zhu, L. Q., Zhang, R. F., Chen, H. N. (2018). Highly air-stable carbon-based α-$CsPbI_3$ perovskite solar cells with a broadened optical spectrum. *ACS Energy Lett.* 3, 1824–1831.

[19] Swarnkar, A., Marshall, A. R., Sanehira, E. M., Chernomordik, B. D., Moore, D. T., Christians, J. A., Chakrabarti, T., Luther, J. M. (2016). Quantum dot-induced phase stabilization of α-$CsPbI_3$ perovskite for high-efficiency photovoltaics. *Science* 354, 92–95.

[20] Tan, S., Yu, B. C., Cui, Y. Q., Meng, F. Q., Huang, C. J., Li, Y. M., Chen, Z. J., Wu, H. J., Shi, J. J., Luo, Y. H., et al. (2022). Temperature-reliable low-dimensional perovskites passivated black-phase $CsPbI_3$ toward stable and efficient photovoltaics. *Angew. Chem. Int. Ed.* 61, e202201300.

[21] Xu, D. F., Wang, J. G., Duan, Y. W., Yang, S. M., Zou, H., Yang, L., Zhang, N., Zhou, H., Lei, X. R., Wu, M. Z., et al. (2023). Highly-stable $CsPbI_3$ perovskite solar cells with an efficiency of 21.11% via fluorinated 4-aminobenzoate cesium bifacial passivation. *Adv. Funct. Mater.* 33, 2304237.

[22] Tan, X., Wang, S. B., Zhang, Q. X., Liu, H. C., Li, W. P., Zhu, L. Q., Chen, H. N. (2023). Stabilizing $CsPbI_3$ perovskite for photovoltaic applications. *Matter* 6, 691–727.

[23] Xu, H. Z., Duan, J. L., Zhao, Y. Y., Jiao, Z. B., He, B. L., Tang, Q. W. (2018). 9.13%-Efficiency and stable inorganic $CsPbBr_3$ solar cells. Lead-free $CsSnBr_{3-x}I_x$ quantum dots promote charge extraction. *J. Power Sources* 399, 76–82.

[24] Kulbak, M., Cahen, D., Hodes, G. (2015). How important is the organic part of lead halide perovskite photovoltaic cells? Efficient $CsPbBr_3$ cells. *J. Phys. Chem. Letters* 6, 2452–2456.

[25] Tong, G. Q., Chen, T. T., Li, H., Qiu, L. B., Liu, Z. H., Dang, Y. Y., Song, W. T., Ono, L. K., Jiang, Y., Qi, Y. B. (2019). Phase transition induced recrystallization and low surface potential barrier leading to 10.91%-efficient $CsPbBr_3$ perovskite solar cells. *Nano Energy* 65, 104015.

[26] Zhou, Q. W., Duan, J. L., Yang, X. Y., Duan, Y. Y., Tang, Q. W. (2020). Interfacial strain release from the $WS_2/CsPbBr_3$ van Der Waals heterostructure for 1.7 V voltage all-inorganic perovskite solar cells. *Angew. Chem.* 132, 22181–22185.

[27] Zhou, Q. W., Duan, J. L., Du, J., Guo, Q. Y., Zhang, Q. Y., Yang, X. Y., Duan, Y. Y., Tang, Q. W. (2021). Tailored lattice "tape" to confine tensile interface for 11.08%-efficiency all-inorganic $CsPbBr_3$ perovskite solar cell with an ultrahigh voltage of 1.702 V. *Adv. Sci.* 8, 2101418.

[28] Duan, J. L., Zhao, Y. Y., Yang, X. Y., Wang, Y. D., He, B. L., Tang, Q. W. (2018). Lanthanide ions doped $CsPbBr_3$ halides for HTM-free 10.14%-efficiency inorganic perovskite solar cell with an ultrahigh open-circuit voltage of 1.594 V. *Adv. Energy Mater.* 8, 1802346.

[29] Nam, J. K., Jung, M. S., Chai, S. U., Choi, Y. J., Kim, D., Park, J. H. (2017). Unveiling the crystal formation of cesium lead mixed-halide perovskites for efficient and stable solar cells. *J. Phys. Chem. Lett.* 8, 2936–2940.

[30] Fu, L., Zhang, Y. N., Chang, B. H., Li, B., Zhou, S. J., Zhang, L. Y., Yin, L. W. (2018). A fluorine-modulated bulk-phase heterojunction and tolerance factor for enhanced performance and structure stability of cesium lead halide perovskite solar cells. *J. Mater. Chem. A* 6, 13263–13270.

[31] Bai, D. L., Zhang, J. R., Jin, Z. W., Bian, H., Wang, K., Wang, H. R., Liang, L., Wang, Q., Liu, S. F. (2018). Interstitial $Mn^{2+}$-driven high-aspect-ratio grain growth for low-trap-density microcrystalline films for record efficiency $CsPbI_2Br$ solar cells. *ACS Energy Lett.* 3, 970–978.

[32] Zeng, Z. B., Zhang, J., Gan, X. L., Sun, H. R., Shang, M. H., Hou, D. G., Lu, C. J., Chen, R. J., Zhu, Y. J., Han, L. Y. (2018). In situ grain boundary functionalization for stable and efficient inorganic $CsPbI_2Br$ perovskite solar cells. *Adv. Energy Mater.* 8, 1801050.

[33] Chen, C. Y., Zhang, F. H., Huang, J., Xue, T., Wang, X., Zheng, C. F., Wang, H., Jia, C. L. (2023). Polymer poly (ethylene oxide) additive for high-stability all-inorganic $CsPbI_{3-x}Br_x$ perovskite solar cells. *Energies* 16, 7849.

[34] Zhao, Y., Zhao, K., Wan, L., Tan, Y. L., Wang, Z. S. (2022). Black phase of inorganic perovskite stabilized with carboxyimidazolium iodide for stable and efficient inverted perovskite solar cells. *ACS Appl. Mater. Interfaces* 14, 6906–6915.

[35] Li, M. H., Liu, S. C., Qiu, F. Z., Zhang, Z. Y., Xue, D. J., Hu, J. S. (2020). High-efficiency $CsPbI_2Br$ perovskite solar cells with dopant-free poly(3-hexylthiophene) hole transporting layers. *Adv. Energy Mater.* 10, 2000501.

[36] Ma, Q. S., Huang, S. J., Wen, X. M., Green, M. A., Ho-Baillie, A. W. Y. (2016). Hole transport layer free inorganic $CsPbIBr_2$ perovskite solar cell by dual source thermal evaporation. *Adv. Energy Mater.* 6, 1502202.

[37] Zhu, W. D., Zhang, Q. N., Chen, D. Z., Zhang, Z. Y., Lin, Z. H., Chang, J. J., Zhang, J. C., Zhang, C. F., Hao, Y. (2018). Intermolecular exchange boosts efficiency of air stable carbon-based all-inorganic plannar $CsPbIBr_2$ perovskite solar cells to over 9%. *Adv. Energy Mater.* 8, 1802080.

[38] Jiang, Y. Z., Yuan, J., Ni, Y. X., Yang, J. E., Wang, Y., Jiu, T., Yuan, M. J., Chen, J. (2018). Reduced-dimensional α-$CsPbX_3$ perovskites for efficient and stable photo-

voltaics. *Joule* 2, 1356–1368.

[39] Liang, J., Zhao, P. Y., Wang, C. X., Wang, Y. R., Hu, Y., Zhu, G. Y., Ma, L. B., Liu, J., Jin, Z. (2017). $CsPb_{0.9}Sn_{0.1}IBr_2$ based all-inorganic perovskite solar cells with exceptional efficiency and stability. *J. Am. Chem. Soc.* 139, 14009–14012.

[40] Wang, X. J., Ran, X. Q., Liu, X. T., Gu, H., Zuo, S. W., Hui, W., Lu, H., Sun, B., Gao, X. Y., Zhang, J., et al. (2020). Tailoring component interaction for air-processed efficient and stable all-inorganic perovskite photovoltaic. *Angew. Chem. Int. Ed.* 59, 13354–13361.

[41] Jiang, H., Feng, J. S., Zhao, H., Li, G. J., Yin, G. N., Han, Y., Yan, F., Liu, Z. K., Liu, S. (2018). Low temperature fabrication for high performance flexible $CsPbI_2Br$ perovskite solar cells. *Adv. Sci.* 5, 1801117.

[42] Iqbal, Z., Félix, R., Musiienko, A., Thiesbrummel, J., Köbler, H., Gutierrez-Partida, E., Gries, T. W., Hüsam, E., Saleh, A., Wilks, R. G., et al. (2024). Unveiling the potential of ambient air annealing for highly efficient inorganic $CsPbI_3$ perovskite solar cells. *J. Am. Chem. Soc.* 146, 4642–4651.

[43] Li, Y., Zhang, Y., Zhu, P., Li, J., Wu, J., Zhang, J., Zhou, X., Jiang, Z., Wang, X., Xu, B., Xu (2023). Achieving 17.46% efficiency $CsPbI_2Br$ perovskite solar cells via multifunction lead chloride-modified ZnO electron transporting layer. *Adv. Funct. Mater.* 33, 2309010.

[44] Duan, X. X., Duan, J. L., Liu, N. M., Li, J. B., Dou, J., Zhang, X. Y., Guo, Q. Y., Wang, Y. L., Wang, Z., Zhao, Y. Y., et al. (2024). Inhibited superoxide-induced halide oxidation with a bioactive factor for stabilized inorganic perovskite solar cells. *SusMat* 4, e233.

[45] Kim, K. S., Jin, I. S., Park, S. H., Lim, S. J., Jung, J. W. (2020). Methylammonium iodide-mediated controlled crystal growth of $CsPbI_2Br$ films for efficient and stable all-inorganic perovskite solar cells. *ACS Appl. Mater. Interfaces* 12, 36228–36236.

[46] Yu, B. C., Zhang, H. Y., Wu, J. H., Li, Y. S., Li, H. S., Li, Y. M.; Shi, J. J., Wu, H. J.; Li, D. M., Luo, Y. H., Meng, Q. B. (2018). Solvent-engineering toward $CsPb(I_xBr_{1-x})_3$ films for high-performance inorganic perovskite solar cells. *J. Mater. Chem. A* 6, 19810–19816.

[47] Almutairi, B. S., Khan, M. I., Mujtaba, A., Subhani, W., Yousef, E. S., Alotaibi, N., Hussain, S., Almaral-Sánchez, J. L. (2024). Impact of La doping on the optoelectronic and structural properties of $CsPbIBr_2$ perovskite solar cell. *Opt. Mater.* 152, 115415.

[48] Khan, U., Rauf, A., Feng, S., Akbar, A. R., Peng, G. Q., Zheng, Q. F., Wu, R. G., Khan, M., Peng, Z. C., Liu, F. D. (2023). Thermally stable and efficient CsF-doped all-inorganic $CsPbIBr_2$ perovskite solar cells exceeding 15% PCE. *Inorg. Chem. Commun.* 153, 110862.

[49] Cheng, J. J., Dong, J. J. (2024). Isobutyramide additive to improve the performance of $CsPbBr_3$ perovskite solar cells prepared by green solvent. *Phys. Status Solidi A-Appl. Mater. Sci.* 221, 2400001.

[50] He, Y. Q., Li, Z. Y., Liu, M. Y., Liu, S. Q., Fu, J. J., Zhang, Y. G., Li, Q. Y., Tong, Y. P., Zheng, Z. (2023). Enhanced performance of $BiI_3$-incorporated $CsPbBr_3$ solar cells. *Dalton Trans.* 52, 17308–17314.

[51] Zhou, L., Guo, X., Lin, Z. H., Ma, J., Su, J., Hu, Z. S., Zhang, C. F., Liu, S., Chang, J. J., Hao, Y. (2019). Interface engineering of low temperature processed all-inorganic $CsPbI_2Br$ perovskite solar cells toward PCE exceeding 14%. *Nano Energy* 60, 583–590.

[52] Yuan, H. W., Zhao, Y. Y., Duan, J. L., Wang, Y. D., Yang, X. Y., Tang, Q. W. (2018). All-inorganic $CsPbBr_3$ perovskite solar cell with 10.26% efficiency by spectra engineering. *J. Mater. Chem. A* 6, 24324–24329.

[53] Yan, D., Lu, X. W., Zhao, S. Y., Zhang, Z. H., Lu, M. X., Feng, J. T., Zhang, J. C., Spencer, K., Watson, T., Li, M., et al. (2022). Lead leaching of perovskite solar cells in aqueous environments: a quantitative investigation. *Solar RRL* 6, 2200332.

[54] Yin, G. N., Zhao, H., Jiang, H., Yuan, S. H., Niu, T. Q., Zhao, K., Liu, Z. K., Liu, S. (2018). Precursor engineering for all-Inorganic $CsPbI_2Br$ perovskite solar cells with 14.78% efficiency. *Adv. Funct. Mater.* 28, 1803269.

[55] Wang, H. S., Sun, J., Gu, Y. S., Xu, C. Q., Lu, Y. W., Hu, J. T., Chen, T., Zhu, C. F., Luo, P. F. (2022). Solvent-engineering-processed $CsPbIBr_2$ inorganic perovskite solar cells with efficiency of ~11%. *Solar Energy Mater. Solar Cells* 238, 111640.

[56] Lee, C., Chae, K., Ko, Y., Lee, C., Kim, T., Park, S., Jung, M. Y., Kim, J., Yun, Y. J., Lee, M., Jun, Y. (2023). Phase stability improvement of a γ-$CsPbI_3$ perovskite solar cell utilizing a Barium Bis(trifluoromethanesulfonimide) solution. *ACS Appl. Mater. Interfaces* 15, 51050–51058.

[57] Dong, C., Han, X. X., Zhao, Y., Li, J. J., Chang, L., Zhao, W. N. (2018). A green anti-solvent process for high performance carbon-based $CsPbI_2Br$ all-inorganic perovskite solar cell. *Solar RRL* 2, 1800139.

[58] Ma, S. P., Lin, F. Y., Luo, Y., Zhu, L., Guo, X. Y., Yang, Y., Null, N., Null, N., Null, N., Null, N., et al. (2022). Formation mechanism of $CsPbBr_3$ in multi-step spin coating process. *Acta Phys. Sin.* 71, 158101.

[59] Zhang, J. H., Wang, Z. W., Mishra, A., Yu, M. L., Shasti, M., Tress, W., Kubicki, D. J., Avalos, C. E., Lu, H. Z., Liu, Y. H., et al. (2020). Intermediate phase enhances inorganic perovskite and metal oxide interface for efficient photovoltaics. *Joule* 4, 507–508.

[60] Wang, J. W., Liu, N., Liu, Z. Y., Liu, J. Y., Zhou, C. Y., Zhang, J., Huang, L. K., Hu, Z. Y., Zhu, Y. J., Liu, X. H. (2024). Versatile self-assembled monolayer enables high-performance inverted $CsPbI_3$ perovskite solar cells. *ACS Appl. Nano Mater.* 7, 15267–15276.

[61] Hu, Y. Q., Bai, F., Liu, X. B., Ji, Q. M., Miao, X. L., Qiu, T., Zhang, S. F. (2017). Bismuth incorporation stabilized α-$CsPbI_3$ for fully inorganic perovskite solar cells. *ACS Energy Lett.* 2, 2219–2227.

[62] Cao, F. R., Tian, W., Wang, M., Cao, H. P., Li, L. (2019). Semitransparent, flexible, and self-powered photodetectors based on ferroelectricity-assisted perovskite nanowire arrays. *Adv. Funct. Mater.* 29, 1901280.

[63] Wang, Y. S., Liu, J. L., Wang, J., Fan, Z. C. (2022). Phase

stability and transformations in $CsSnI_3$: Is anharmonicity negligible. *J. Phys. Chem. C* 126, 19470–19479.

[64] Jokar, E., Chien, C. H., Tsai, C. M., Fathi, A., Diau, E. W. G. (2019). Robust tin-based perovskite solar cells with hybrid organic cations to attain efficiency approaching 10%. *Adv. Mater.* 31, 1804835.

[65] Kumar, M. H., Dharani, S., Leong, W. L., Boix, P. P., Prabhakar, R. R., Baikie, T., Shi, C., Ding, H., Ramesh, R., Asta, M., et al. (2014). Lead-free halide perovskite solar cells with high photocurrents realized through vacancy modulation. *Adv. Mater.* 26, 7122–7127.

[66] Marshall, K. P., Walker, M., Walton, R. I., Hatton, R. A. (2016). Enhanced stability and efficiency in hole-transport-layer-free $CsSnI_3$ perovskite photovoltaics. *Nature Energy* 1, 16178.

[67] Sun, Q., Gu, A. J., Yu, H. X., Shen, Y., Wang, M. K. (2023). A single crystal derived precursor for improving the performance of $CsSnI_3$ perovskite solar cells. *J. Mater. Chem. A* 11, 17292–17297.

[68] Shao, S. Y., Dong, J. J., Duim, H., Ten Brink, G. H., Blake, G. R., Portale, G., Loi, M. A. (2019). Enhancing the crystallinity and perfecting the orientation of formamidinium tin iodide for highly efficient Sn-based perovskite solar cells. *Nano Energy* 60, 810–816.

[69] Wang, N., Zhou, Y. Y., Ju, M. G., Pang, S. P. (2016). Heterojunction-depleted lead-free perovskite solar cells with coarse-grained B-γ-$CsSnI_3$ thin films. *Adv. Energy Mater.* 6, 1601130.

[70] Sabba, D., Mulmudi, H. K., Prabhakar, R. R., Krishnamoorthy, T., Baikie, T., Boix, P. P., Mhaisalkar, S., Mathews, N. (2015). Impact of anionic $Br^-$ substitution on open circuit voltage in lead free perovskite ($CsSnI_{3-x}Br_x$) solar cells. *J. Phys. Chem. C* 119, 1763–1767.

[71] Jaroenjittichai, A. P., Laosiritaworn, Y. (2018). Band alignment of cesium-based halide perovskites. *Ceram. Int.* 44, S161–S163.

[72] Kumar, A., Pandey, N., Punetha, D., Saha, R., Chakrabarti, S. (2023). Enhancement in the structural and optical properties after incorporation of reduced graphene oxide (rGO) nanocomposite in pristine $CsSnBr_3$ for solar cell application. *ACS Appl. Electron. Mater.* 5, 3144–3153.

[73] Kholil, M. I., Bhuiyan, M. T. H., Rahman, M. A., Ali, M. S., Aftabuzzaman, M. (2021). Influence of molybdenum and technetium doping on visible light absorption, optical and electronic properties of lead-free perovskite $CsSnBr_3$ for optoelectronic applications. *RSC Adv.* 11, 2405–2414.

[74] Raoui, Y., Ez-Zahraouy, H., Ahmad, S., Kazim, S. (2021). Unravelling the theoretical window to fabricate high performance inorganic perovskite solar cells. *Sustain. Energy Fuels* 5, 219–229.

[75] Duan, Q. Q., Ji, J. Y., Hong, X., Fu, Y. C., Wang, C. Y., Zhou, K., Liu, X. Q., Yang, H., Wang, Z. Y. (2020). Design of hole-transport-material free $CH_3NH_3PbI_3$/$CsSnI_3$ all-perovskite heterojunction efficient solar cells by device simulation. *Solar Energy* 201, 555–560.

[76] Li, X. R., Zhou, H. Y., Zhang, J. F., Sang, K. H., Fan, H., Lu, J. Y., Pang, Q., Chen, P. C., Zhou, L. Y., Li, L., et al. (2023). Trans-spatial structure additive passivated Sn (II) for high-efficiency $CsSnI_3$ perovskite solar cells fabricated in humid air. *Chem. Nanomat.* 9, e202200481.

[77] Xiao, Z. W., Zhou, Y. Y., Hosono, H., Kamiya, T. (2015). Intrinsic defects in a photovoltaic perovskite variant $Cs_2SnI_6$. *Phys. Chem. Chem. Phys.* 17, 18900–18903.

[78] Fang, D., Tan, Y. F., Ren, Y. X., Zheng, S. C., Xiong, F. M., Wang, A. C., Chang, K., Mi, B. X., Cao, D. P., Gao, Z. Q. (2023). Simple solution preparation of $Cs_2SnI_6$ films and their applications in solid-state DSSCs. *ACS Appl. Mater. Interfaces* 15, 32538–32551.

[79] Xiao, Z. W., Zhou, Y. Y., Hosono, H., Kamiya, T., Padture, N. P. (2018). Bandgap optimization of perovskite semiconductors for photovoltaic applications. *Chem. -A Eur. J.* 24, 2305–2316.

[80] Lee, B., Krenselewski, A., Baik, S. I., Seidman, D. N., Chang, R. P. H. (2017). Solution processing of air-stable molecular semiconducting iodosalts, $Cs_2SnI_{6-x}Br_x$, for potential solar cell applications. *Sustain. Energy Fuels* 1, 710–724.

[81] Pujiarti, H., Hidayat, R., Wulandari, P. (2020). Effect of lead-free perovskite $Cs_2SnI_6$ addition in the structure of dye-sensitized solar cell. *Key Eng. Mater.* 860, 22–27.

[82] Ullah, S., Ullah, S., Wang, J. M., Yang, S. E., Xia, T. Y., Guo, H. Z., Chen, Y. S. (2020). Investigation of air-stable $Cs_2SnI_6$ films prepared by the modified two-step process for lead-free perovskite solar cells. *Semicond. Sci. Technol.* 35, 125027.

[83] Yousefzadeh, F., Ghanbari, M., Dawi, E. A., Salavati-Niasari, M. (2023). $Cs_2SnI_6$ perovskites nanostructures as excellent photocatalytic degradation of organic dye pollutants in water under visible light: synthesis and characterization. *Arabian J. Chem.* 16, 104904.

[84] Murshed, R., Thornton, S., Walkons, C., Koh, J. J., Bansal, S. (2023). $SnF_2$-doped $Cs_2SnI_6$ ordered vacancy double perovskite for photovoltaic applications. *Solar RRL* 7, 2300165.

[85] Chauhan, V., Tripathi, D., Singh, P., Sharma, A., Khanna, M. K., Kumar, R., Bhatnagar, R., Kumar, T. (2023). Prospects for lead free perovskite for photovoltaic applications and biological impacts: challenges and opportunities. *Inorg. Chem. Commun.* 157, 111421.

[86] Kumari, D., Jaiswal, N., Shukla, R., Punetha, D., Pandey, S. K., Pandey, S. K. (2023). Design and fabrication of all-inorganic transport materials-based $Cs_2SnI_6$ perovskite solar cells. *J. Mater. Sci.: Mater. Electron.* 34, 1792.

[87] Ke, J. C. R., Lewis, D. J., Walton, A. S., Spencer, B. F., O'Brien, P., Thomas, A. G., Flavell, W. R. (2018). Ambient-air-stable inorganic $Cs_2SnI_6$ double perovskite thin films *via* aerosol-assisted chemical vapour deposition. *J. Mater. Chem. A* 6, 11205–11214.

[88] Wang, G. Q., Cheng, L., Bi, J. Y., Chang, J. R., Meng, F. N. (2024). B-site doping with bismuth ion enhances the efficiency and stability of inorganic $CsSnI_3$ perovskite solar cell. *Mater. Lett.* 354, 135394.

[89] Li, W. Z., Li, J. W., Li, J. L., Fan, J. D., Mai, Y. H., Wang, L. D. (2016). Addictive-assisted construction of all-inorganic $CsSnIBr_2$ mesoscopic perovskite solar cells with superior thermal stability up to 473 K. *J. Mater. Chem. A* 4, 17104–17110.

[90] Ding, W., Bai, C., Ren, Y. X., Fang, D., Bai, J., Wen, J. L., Mi, B. X., Cao, D. P., Gao, Z. Q. (2024). Synergetic effects of recombination-blocking, band-Bending and gap-state manipulation by interfacial engineering in solid-state DSSCs comprising $Cs_2SnI_6$ electrolyte. *Surf. Interfaces* 48, 104246.

[91] Ban, H. X., Nakajima, T., Liu, Z. R., Yu, H. X., Sun, Q., Dai, L. T., Shen, Y., Zhang, X. L., Zhu, J., Chen, P., et al. (2022). Over 8% efficient $CsSnI_3$-based mesoporous perovskite solar cells enabled by two-step thermal annealing and surface cationic coordination dual treatment. *J. Mater. Chem. A* 10, 3642–3649.

[92] Dai, L. T., Cabarrocas, P. R. I., Ban, H. X., Zhang, Z. G., Sun, Q., Li, X. J., Gu, A. J., Yang, W. P., Yu, H. X., Shen, Y., et al. (2023). Single-crystal nanowire cesium tin triiodide perovskite solar cell. *Small* 19, 2208062.

[93] Qamar, S., Sultan, M., Akhter, Z., Ela, S. E. (2022). A facile one-step solution synthesis of $Cs_2SnI_{6-x}Br_x$ using less-toxic methanol solvent for application in dye-sensitized solar cells. *Int. J. Energy Res.* 46, 13441–13452.

[94] Zhang, Z. G., Sun, Q., Nakajima, T., Ban, H. X., Liu, Z. R., Yu, H. X., Wang, Y., Xiao, Z. W., Shen, Y., Wang, M. K. (2022). Achieving efficient and stable inorganic $CsSnI_3$ mesoporous perovskite solar cells *via* galvanic displacement reaction. *J. Mater. Chem. A* 10, 23204–23211.

[95] Zhang, W. H., Cai, Y. T., Liu, H., Xia, Y., Cui, J. S., Shi, Y. Q., Chen, R., Shi, T. T., Wang, H. L. (2022). Organic-free and lead-free perovskite solar cells with efficiency over 11%. *Adv. Energy Mater.* 12, 2202491.

[96] Unger, E. L., Kegelmann, L., Suchan, K., Sörell, D., Korte, L., Albrecht, S. (2017). Roadmap and roadblocks for the band gap tunability of metal halide perovskites. *J. Mater. Chem. A* 5, 11401–11409.

[97] Wang, Q. Q., Guo, K. Y., Gu, S. W., Huang, W., Peng, H., Wu, W. P., Ding, J. N. Electrical performance, loss analysis, and efficiency potential of industrial-type PERC, TOPCon, and SHJ solar cells: a comparative study. *Prog. Photovoltaics* in press.

[98] Casey, J. P. (2024). Longi Unveils Hbc Cell With Record 27.3% conversion efficiency. https://www.pv-tech.org/longi-heterojunction-back-contact-cell-27-3-conversion-efficiency/ (accessed 5 July, 2024)

[99] Chen, B., Zheng, X. P., Bai, Y., Padture, N. P., Huang, J. S. (2017). Progress in tandem solar cells based on hybrid organic-inorganic perovskites. *Adv. Energy Mater.* 7, 1602400.

[100] Leijtens, T., Bush, K. A., Prasanna, R., McGehee, M. D. (2018). Opportunities and challenges for tandem solar cells using metal halide perovskite semiconductors. *Nat. Energy* 3, 828–838.

[101] Yu, Z. S., Leilaeioun, M., Holman, Z. (2016). Selecting tandem partners for silicon solar cells. *Nat. Energy* 1, 16137.

[102] Wang, Z. Y., Song, Z. N., Yan, Y. F., Liu, S. Z., Yang, D. (2019). Perovskite-a perfect top cell for tandem devices to break the S-Q limit. *Adv. Sci.* 6, 1801704.

[103] Yu, Z. J., Fisher, K. C., Wheelwright, B. M., Angel, R. P., Holman, Z. C. (2015). PVMirror: a new concept for tandem solar cells and hybrid solar converters. *IEEE J. Photovoltaics* 5, 1791–1799.

[104] Li, H., Zhang, W. (2020). Perovskite tandem solar cells: from fundamentals to commercial deployment. *Chem. Rev.* 120, 9835–9950.

[105] Hou, F. H., Han, C., Isabella, O., Yan, L. L., Shi, B., Chen, J. F., An, S. C., Zhou, Z. X., Huang, W., Ren, H. Z., et al. (2019). Inverted pyramidally-textured PDMS antireflective foils for perovskite/silicon tandem solar cells with flat top cell. *Nano Energy* 56, 234–240.

[106] Jošt, M., Köhnen, E., Morales-Vilches, A. B., Lipovšek, B., Jäger, K., Macco, B., Al-Ashouri, A., Krč, J., Korte, L., Rech, B., et al. (2018). Textured interfaces in monolithic perovskite/silicon tandem solar cells: advanced light management for improved efficiency and energy yield. *Energy Environ. Sci.* 11, 3511–3523.

[107] Zheng, J. H., Mehrvarz, H., Liao, C., Bing, J. M., Cui, X., Li, Y., Gonçales, V. R., Lau, C. F. J., Lee, D. S., Li, Y., et al. (2019). Large-area 23%-efficient monolithic perovskite/homojunction-silicon tandem solar cell with enhanced UV stability using down-shifting material. *ACS Energy Lett.* 4, 2623–2631.

[108] Sahli, F., Werner, J., Kamino, B. A., Bräuninger, M., Monnard, R., Paviet-Salomon, B., Barraud, L., Ding, L., Diaz Leon, J. J., Sacchetto, D., et al. (2018). Fully textured monolithic perovskite/silicon tandem solar cells with 25.2% power conversion efficiency. *Nat. Mater.* 17, 820–826.

[109] Tockhorn, P., Sutter, J., Cruz, A., Wagner, P., Jäger, K., Yoo, D., Lang, F., Grischek, M., Li, B., Al-Ashouri, A., et al. (2022). Nano-optical designs enhance monolithic perovskite/silicon tandem solar cells toward 29.8% efficiency. https://scholar.google.es/citations?view_op=view_citation&hl=th&user=slgVcEMAAAAJ&citation_for_view=slgVcEMAAAAJ:W7OEmFMy1HYC, 2022 (accessed 5 July 2024).

[110] Isikgor, F. H., Furlan, F., Liu, J., Ugur, E., Eswaran, M. K., Subbiah, A. S., Yengel, E., De Bastiani, M., Harrison, G. T., Zhumagali, S., et al. (2021). Concurrent cationic and anionic perovskite defect passivation enables 27.4% perovskite/silicon tandems with suppression of halide segregation. *Joule* 5, 1566–1586.

[111] Roß, M., Severin, S., Stutz, M. B., Wagner, P., Köbler, H., Favin-Lévêque, M., Al-ashouri, A., Korb, P., Tockhorn, P., Abate, A., et al. (2021). Co-evaporated formamidinium lead iodide based perovskites with 1000 h constant stability for fully textured monolithic perovskite/silicon tandem solar cells. *Adv. Energy Mater.* 11, 2101460.

[112] Tockhorn, P., Sutter, J., Cruz, A., Wagner, P., Jäger, K., Yoo, D., Lang, F., Grischek, M., Li, B. R., Li, J. Z., et al. (2022). Nano-optical designs for high-efficiency mono-

lithic perovskite-silicon tandem solar cells. *Nat. Nanotechnol.* 17, 1214–1221.

[113] Morales-Masis, M., De Wolf, S., Woods-Robinson, R., Ager, J. W., Ballif, C. (2017). Transparent electrodes for efficient optoelectronics. *Adv. Electron. Mater.* 3, 1600529.

[114] Aydin, E., De Bastiani, M., Yang, X. B., Sajjad, M. (2019). Zr-doped indium oxide (IZRO) transparent electrodes for perovskite-based tandem solar cells. *Adv. Funct. Mater.* 29, 1901741.

[115] Jiang, Y., Feurer, T., Carron, R., Sevilla, G. T., Moser, T., Pisoni, S., Erni, R., Rossell, M. D., Ochoa, M., Hertwig, R., et al. (2020). High-mobility $In_2O_3$:H electrodes for four-terminal perovskite/$CuInSe_2$ tandem solar cells. *ACS Nano* 14, 7502–7512.

[116] Jošt, M., Kegelmann, L., Korte, L., Albrecht, S. (2020). Monolithic perovskite tandem solar cells: a review of the present status and advanced characterization methods toward 30% efficiency. *Adv. Energy Mater.* 10, 1904102.

[117] Chauhan, S., Singh, R. (2023). Investigation of 2T Pb-free wide bandgap perovskite/c-Si tandem device through simulation by SCAPS-1D. *Sādhanā* 48, 40.

[118] Werner, J., Weng, C. H., Walter, A., Fesquet, L., Seif, J. P., De Wolf, S., Niesen, B., Ballif, C. (2016). Efficient monolithic perovskite/silicon tandem solar cell with cell area >1 $cm^2$. *J. Phys. Chem. Letters* 7, 161–166.

[119] Al-Ashouri, A., Köhnen, E., Li, B. R., Magomedov, A., Hempel, H., Caprioglio, P., Márquez, J. A., Morales Vilches, A. B., Kasparavicius, E., Smith, J. A., et al. (2020). Monolithic perovskite/silicon tandem solar cell with >29% efficiency by enhanced hole extraction. *Science* 370, 1300–1309.

[120] Mishima, R., Hino, M., Kanematsu, M., Kishimoto, K., Ishibashi, H., Konishi, K., Okamoto, S., Irie, T., Fujimoto, T., Yoshida, W., et al. (2022). 28.3% efficient perovskite-silicon tandem solar cells with mixed self-assembled monolayers. *Appl. Phys. Express* 15, 076503.

[121] Wu, B., Ning, W. H., Xu, Q. A., Manjappa, M., Feng, M. J., Ye, S. Y., Fu, J. H., Lie, S., Yin, T. T., Wang, F., et al. (2021). Strong self-trapping by deformation potential limits photovoltaic performance in bismuth double perovskite. *Sci. Adv.* 7, eabd3160.

[122] Jung, H., Kim, G., Jang, G. S., Lim, J., Kim, M., Moon, C. S., Hao, X. J., Jeon, N. J., Yun, J. S., Park, H. H., et al. (2021). Transparent electrodes with enhanced infrared transmittance for semitransparent and four-terminal tandem perovskite solar cells. *ACS Appl. Mater. Interfaces* 13, 30497–30503.

[123] Uzum, A., Kanda, H., Ito, S. (2015). Perovskite/crystalline silicon tandem solar cells fabricated by non-vacuum-process. In Proceedings of the 42nd IEEE Photovoltaic Specialist Conference (PVSC). Beijing, p 1–4.

[124] Zhang, M. R., Zhu, Z. W., Yang, X. Q., Yu, T. X., Yu, X. Q., Lu, D., Li, S. F., Zhou, D. Y., Yang, H. (2023). Research progress of perovskite/crystalline silicon tandem solar cells with efficiency of over 30% (in Chinese). *Acta Phys. Sin.* 72, 058801.

[125] Mailoa, J. P., Bailie, C. D., Johlin, E. C., Hoke, E. T., Akey, A. J., Nguyen, W. H., McGehee, M. D., Buonassisi, T. (2015). A 2-terminal perovskite/silicon multijunction solar cell enabled by a silicon tunnel junction. *Appl. Phys. Lett.* 106, 121105.

[126] Sahli, F., Kamino, B. A., Werner, J., Bräuninger, M., Paviet-Salomon, B., Barraud, L., Monnard, R., Seif, J. P., Tomasi, A., Jeangros, Q., et al. (2018). Improved optics in monolithic perovskite/silicon tandem solar cells with a nanocrystalline silicon recombination junction. *Adv. Energy Mater.* 8, 1701609.

[127] Rolland, A., Pedesseau, L., Huang, Y., Wang, S., Sapori, D., Cornet, C., Durand, O., Even, J., Kepenekian, M., Katan, C. (2017). Computational design of high performance hybrid perovskite on silicon 2-T tandem solar cells based on a tunnel junction. In Proceedings of the 2017 International Conference on Numerical Simulation of Optoelectronic Devices. Copenhagen, Denmark, p 67–68.

[128] Chen, B., Yu, Z. S., Liu, K., Zheng, X. P., Liu, Y., Shi, J. W., Spronk, D., Rudd, P. N., Holman, Z., Huang, J. S. (2019). Grain engineering for perovskite/silicon monolithic tandem solar cells with efficiency of 25.4%. *Joule* 3, 177–190.

[129] Xu, J. X., Boyd, C. C., Yu, Z. J., Palmstrom, A. F., Witter, D. J., Larson, B. W., France, R. M., Werner, J., Harvey, S. P., Wolf, E. J., et al. (2020). Triple-halide wide–band gap perovskites with suppressed phase segregation for efficient tandems. *Science* 367, 1097–1104.

[130] Qiu, Z. W., Xu, Z. Q., Li, N. X., Zhou, N., Chen, Y. H., Wan, X. X., Liu, J. L., Li, N., Hao, X. T., Bi, P. Q., et al. (2018). Monolithic perovskite/Si tandem solar cells exceeding 22% efficiency via optimizing top cell absorber. *Nano Energy* 53, 798–807.

[131] Zhu, S. J., Hou, F. H., Huang, W., Yao, X., Shi, B., Ren, Q. S., Chen, J. F., Yan, L. L., An, S. C., Zhou, Z. X., et al. (2018). Solvent engineering to balance light absorbance and transmittance in perovskite for tandem solar cells. *Solar RRL* 2, 1800176.

[132] Kim, C. U., Yu, J. C., Jung, E. D., Choi, I. Y., Park, W., Lee, H., Kim, I., Lee, D. K., Hong, K. K., Song, M. H., et al. (2019). Optimization of device design for low cost and high efficiency planar monolithic perovskite/silicon tandem solar cells. *Nano Energy* 60, 213–221.

[133] Islam, M. T., Jani, M. R., Islam, A. F., Shorowordi, K. M., Chowdhury, S., Nishat, S. S., Ahmed, S. (2021). Investigation of $CsSn_{0.5}Ge_{0.5}I_3$-on-Si tandem solar device utilizing SCAPS simulation. *IEEE Trans. Electron Devices* 68, 618–625.

[134] Azadinia, M., Ameri, M., Ghahrizjani, R. T., Fathollahi, M. (2021). Maximizing the performance of single and multijunction MA and lead-free perovskite solar cell. *Mater. Today Energy* 20, 100647.

[135] Jayan, K. D., Laref, A. (2023). High-efficiency Cs-based perovskite-silicon tandem solar cells-a modeling study. *Phys. Status Solidi A- Appl. Mater. Sci.* 220, 2200622.

[136] Hossain, M. J., Hossain, M. (2023). Over 32% efficient all-inorganic two-terminal $CsPbI_2Br$/Si tandem solar cells: a

numerical investigation. *Energy Technol.* 11, 2201297.

[137] Wang, S. L., Wang, P. Y., Chen, B. B., Li, R. J., Ren, N. Y., Li, Y. C., Shi. B., Huang, Q., Zhao, Y., Grätzel, M., et al. (2022). Suppressed recombination for monolithic inorganic perovskite/silicon tandem solar cells with an approximate efficiency of 23%. *eScience* 2, 339–346.

[138] Wang, S. L., Wang, P. Y., Shi, B., Sun, C., Sun, H. R., Qi, S. S., Huang, Q., Xu, S. Z., Zhao, Y., Zhang, X. D. (2023). Inorganic perovskite surface reconfiguration for stable inverted solar cells with 20.38% efficiency and its application in tandem devices. *Adv. Mater.* 35, 2300581.